Improved convective ice microphysics parameterization in the NCAR CAM model

Lin Lin[1], Qiang Fu[2], Xiaohong Liu[1,*], Yunpeng Shan[3], Scott E. Giangrande[3], Gregory S. Elsaesser[4], Kang Yang[5], and Dié Wang[3]

[1]Department of Atmospheric Sciences, Texas A&M University, College Station, TX

[2]Department of Atmospheric Sciences, University of Washington, Seattle, WA

[3]Department of Environment and Climate Sciences, Brookhaven National Laboratory, Upton, NY

[4]Department of Applied Physics and Mathematics, Columbia University, and NASA Goddard Institute for Space Studies, New York City, NY

[5]Department of Atmospheric and Oceanic Sciences, University of Colorado and Laboratory for Atmospheric and Space Physics, Boulder, CO

*Correspondence to: Xiaohong Liu (xiaohong.liu@tamu.edu)

Key points:

- Graupel is added to a convective microphysics scheme for global climate models
- New convective ice particle terminal velocity schemes are implemented and convective snow is allowed to detrain
- Vertical distribution of ice mass in the mid- and upper-troposphere is improved

Abstract

Partitioning deep convective cloud condensates into components that sediment and detrain, known to be a challenge for global climate models, is important for cloud vertical distribution and anvil cloud formation. In this study, we address this issue by improving the convective microphysics scheme in the National Center for Atmospheric Research Community Atmosphere Model version 5.3 (CAM5.3). The improvements include: (1) considering sedimentation for cloud ice crystals that do not fall in the original scheme, (2) applying a new terminal velocity parameterization that depends on the environmental conditions for convective snow, (3) adding a new hydrometeor category, "rimed ice", to the original four-class (cloud liquid, cloud ice, rain, and snow) scheme, and (4) allowing convective clouds to detrain snow particles into stratiform clouds.

Results from the default and modified CAM5.3 models were evaluated against observations from the U.S. Department of Energy Tropical Warm Pool–International Cloud Experiment (TWP-ICE) field campaign. The default model overestimates ice amount, which is largely attributed to the underestimation of convective ice particle sedimentation. By considering cloud ice sedimentation and rimed ice particles and applying a new convective snow terminal velocity parameterization, the vertical distribution of ice amount is much improved in the mid- and upper-troposphere when compared to observations. The vertical distribution of ice condensate also agrees well with observational best estimates upon considering snow detrainment. Comparison with observed convective updrafts reveals that current bulk model fails to reproduce the observed updraft magnitude and occurrence frequency, suggesting spectral distributions be required to simulate the subgrid updraft heterogeneity.

Keywords: microphysics parameterization, convective clouds, terminal velocity, detrainment, updraft

1. Introduction

While clouds are of importance in determining Earth's radiative energy balance, they are among the largest contributors to uncertainty in simulations of weather and climate. Despite increased computational power, cloud microphysical processes are still represented by parameterizations even in high-resolution models due to the fact that these processes are complicated and cannot be resolved. A continuing research effort to improve cloud microphysics parameterizations is needed.

Global climate models (GCMs) treat convective and stratiform clouds separately due in part to the coarse grid spacing (e.g., 100~200 km) and drastically different temporal/spatial scales for each cloud type. Treatment of stratiform clouds includes the stratiform cloud microphysics parameterizations (e.g., Fowler et al., 1996; Lohmann and Roeckner, 1996; Morrison and Gettelman, 2008) that simulate the evolution of cloud hydrometeors based on detailed microphysical process rates. In contrast, cumulus microphysics in most convection schemes is often ignored or oversimplified. Previous studies showed a high dependence of climate sensitivity on the treatment of convection in models (Slingo et al., 1994). The simplified convective microphysics parameterizations have raised concerns about the adequacy for climate studies. Thus, improving the parameterizations of convection and associated microphysical processes is still one of the major tasks in GCM development (e.g., Danabasoglu et al., 2020; Elsaesser et al., 2017; Golaz et al., 2019).

Convection parameterizations are conceptualized in a variety of ways (e.g., see Chapter 6 in Stensrud, 2007). Some parameterizations relate convective activity to large-scale moisture convergence (e.g., Kuo 1965; 1974); some are based on moist convective adjustment (e.g., Betts, 1986) and some use convective instability-based mass flux schemes (e.g., Arakawa and Schubert, 1974; Zhang and McFarlane, 1995). Nearly all of these parameterizations are designed to represent the thermodynamic influence of convection on the large-scale moisture and heat budget, but with a rather crude treatment of cloud microphysics processes. In the early convection schemes, for example, conversion of cloud water to rainwater was determined by empirical relationships with tuning parameters. Later, single-moment microphysics schemes for convective clouds emerged that incorporated the microphysical processes to varying degrees. Recently, GCMs have started to incorporate detailed double-moment convective cloud microphysics schemes (Zhang and Song, 2016) that explicitly treat mass mixing ratios and number concentrations of convective cloud hydrometeors (e.g., Song and Zhang, 2011, hereafter SZ11; Zhang et al., 2005). With these convective microphysics schemes, a new door opened for studies of convective precipitation formation, convection-stratiform interactions, and aerosol-convection-precipitation interactions (e.g., Tao et al., 2012).

Most current convective microphysics schemes (e.g., SZ11; Zhang et al., 2005) used in GCMs are developed based on stratiform microphysics schemes (e.g., Lohmann and Roeckner, 1996; Morrison and Gettelman, 2008, hereafter MG08), partly owing to incomplete knowledge of cumulus microphysics and lack of observations within convective cores. Though the ultimate goal for representing clouds is to develop a unified cloud scheme for both convective and stratiform clouds, we note that those expressions in the stratiform microphysics scheme are uncertain especially when applied to cloud types other than stratiform. Convective cloud microphysical processes can be very different from stratiform because of the very different dynamic and thermodynamic controls (Heymsfield et al., 2013; Houze, 1997; Jackson et al., 2017). For example, the representation of convective hydrometeor terminal velocities are likely different from that in stratiform clouds because of different particle microphysical properties (e.g., size, density, habit).

Among the microphysical processes, riming is the one by which ice particles collect supercooled cloud water to form rimed ice particles. In contrast to stratiform clouds where rimed ice hydrometeors may not be important (Gettelman et al., 2019), deep convection provides a more favorable environment for producing a large number of rimed ice hydrometeors characterized by appreciable fall speeds. The rimed ice hydrometeors are often neglected in GCM convective microphysics parameterizations, but can be important for properly simulating convective cloud properties (e.g., vertical distribution of cloud water, cloud vertical extent, updraft intensity, and precipitation rate).

Ice water content (IWC) is an important cloud microphysical property, yet GCM simulations do not agree on its magnitude and spatial distribution (Jiang et al., 2012; Li et al., 2012; Waliser et al., 2009). Vertical IWC distributions in convective clouds depend on the partitioning of convective cloud condensate into precipitation and detrained components. The latter is a major source for the formation of anvil clouds. Because of their large areal coverage, these anvil clouds are an important radiation modulator. However, their control on Earth’s radiation energy budget and their responses to climate change remain highly uncertain (Bony et al., 2006; Fu et al., 1995; Hartmann, 2016; Hartmann and Larson, 2002; Lindzen et al., 2001; Ramanathan and Collins, 1991; Stephens, 2005). Additionally, the detrainment of convective cloud condensates may be underestimated (Storer et al., 2015) in GCMs since most GCM convective microphysics schemes (e.g., SZ11) do not consider the detrainment of precipitating particles (e.g., rain and snow). The snow particles that dominate the total ice mass have a far slower fall speed than raindrops that have the same size, suggesting that snow detrainment should be considered. The magnitude of detrained condensate also depends on the competition between condensate lofted by convective updrafts and that which falls out. It is therefore critically important to reliably represent both convective updraft speeds and convective hydrometeor terminal velocities in GCMs.

An empirical pre-defined terminal velocity-diameter (V_t-D) power-law relationship ($V_t = \alpha D^{\beta}$) is often used to represent how fast an individual ice particle with diameter D will fall. The pre-factor (α) and exponential factor (β) are determined from fits to experimental and field campaign aircraft datasets (e.g., Gunn and Kinzer, 1949; Heymsfield, 1972; Locatelli and Hobbs, 1974). Often, these V_t-D relationships with constant α and β coefficients are inappropriately extrapolated well beyond the subranges of the size spectra within which these measurements were made. Meanwhile, these oversimplified power-law relationships are often deficient. For instance, V_t decreases unrealistically when an ice particle becomes smaller but denser. The V_t-D relationship with constant α and β lacks degrees of freedom to account for natural variability. Recently, Elsaesser et al. (2017, hereafter EL17) developed a new parameterization of convective ice particle terminal velocity based on *in situ* aircraft observations in flight legs adjacent to convective cores collected during several U.S. Department of Energy (DOE) and NASA campaigns. The EL17 parameterization is unique in that it does not assume an ice particle habit. Coefficients α and β in EL17 vary as a function of temperature, pressure and IWC.

In this study, we introduce several improvements to the SZ11 convective microphysics scheme in the National Center for Atmospheric Research (NCAR) Community Atmosphere Model version 5.3 (CAM5.3) with a focus on ice microphysics. The modifications include 1) the addition of the rimed ice category; we use the term "rimed ice" to refer to graupel in the rest of the manuscript; 2) the implementation of the EL17 terminal velocity parameterization for convective snow and rimed ice particles; 3) the application of a new terminal velocity parameterization formulated in terms of the *Davis* or *Best* (X) and *Reynolds* (Re) numbers for convective cloud ice particles; and 4) the detrainment of convective snow to feed into the stratiform cloud microphysics. Simulated convective updraft vertical velocity within convective cores is also evaluated against ground-based radar retrievals. The rest of the manuscript is organized as follows. Development of parameterizations and model configuration are presented in section 2. Observational datasets used for model evaluation are described in section 3. Results are discussed in section 4, and section 5 summarizes the findings.

2. Model and Parameterizations

2.1 The CAM5.3 with default convective microphysics parameterization

The NCAR CAM5.3 is the atmosphere component of the Community Earth System Model version 1.2 (Hurrell et al., 2013). In the standard CAM5.3, stratiform cloud microphysical processes for different hydrometeors (i.e., cloud water, cloud ice, rain and snow) are treated by a double-moment stratiform microphysics scheme (MG08). For MG08, the mass mixing ratios and number concentrations of cloud droplets and cloud ice are prognostic, while those of rain and snow are diagnosed. Deep convection is represented by a mass-flux convection scheme developed by Zhang and McFarlane (1995, hereafter ZM95). Detailed microphysical processes such as activation of cloud droplets on aerosols, ice nucleation, and cloud hydrometeor collection processes to form precipitating particles are crudely parameterized or neglected in ZM95. Total cloud water condensate is determined by net condensation within updraft plumes, and the partitioning between liquid and ice is determined by a simple linear function of temperature.

SZ11 developed a double-moment microphysics scheme similar to MG08 and implemented it into ZM95 to represent convective cloud microphysics. SZ11 explicitly treats mass mixing ratios and number concentrations of cloud liquid, cloud ice, rain, and snow by considering detailed microphysical processes such as autoconversion, accretion, homogeneous and heterogeneous freezing, rain and snow sedimentation, ice nucleation, and droplet activation. Convective updraft vertical velocity, calculated from the updraft kinetic energy budget equation (see SZ11 for more details), is used to parameterize the activations of cloud condensation nuclei and ice nuclei (e.g., Liu et al., 2007). Moreover, cloud liquid and cloud ice are assumed to remain suspended, and only precipitating particles (rain and snow) are allowed to sediment. On the other hand, cloud liquid and cloud ice detrain, whereas precipitating particles including snow do not. The standard CAM5.3 physics package, together with the SZ11 convective microphysics scheme, are used for the control simulation (CTRL) in this study.

2.2 Improved convective microphysics parameterization

Improved convective ice microphysics parameterizations to the SZ11 scheme are presented in this section. Figure 1 shows a schematic diagram for the microphysical processes that are considered. The modified and added processes are shown in blue.

2.2.1 Terminal velocity (V_t-D) parameterizations

The EL17 parameterization is used to replace the original representation of terminal velocities of snow in SZ11 (and is also used to represent terminal velocities of rimed ice particles, as detailed below). The terminal velocity parameterization based on *X* and *Re* numbers has been described extensively in the literature (Heymsfield and Westbrook, 2010; Lamb and Verlinde, 2011; Pruppacher and Klett, 1997) but has not been tested in GCMs. In this study, we use the *X-Re* terminal velocity parameterization for representing the terminal velocity of cloud ice. We primarily maintain the V_t-D power-law relationship forms (i.e., $V_t = \alpha D^{\beta}$) to parameterize ice particle fall speeds, wherein α and β coefficients are no longer prescribed, but are derived as a function of environment and ice mass. Below, we briefly summarize both schemes.

The EL17 scheme is developed through the use of *in situ* ice particle data for particles larger than 50 μm (threshold chosen to mitigate shattering effects and instrument uncertainty on the measurement of small ice particles), indicating that this scheme is suitable for calculating the snow and rimed ice particle fall speeds in bulk cloud microphysical schemes. Since the fall speed is dependent on temperature, pressure and IWC, it is expected to simulate increased fall speeds for larger ice particles with higher IWC falling at warmer temperatures and lower altitudes. This leads to a more efficient removal of cloud condensates in the lower troposphere and a longer lifetime of ice particles aloft. Coefficients α and β in the EL17 *Vt-D* parameterizations are summarized in Table 1. The terminal velocity coefficients of rimed ice particles (not provided in EL17) are given in Table E1 of Appendix E. These coefficients were derived by recomputing the fits to the campaign data in EL17 with the constraint that they transit to the dense ice formulation in Heymsfield and Wright (2014) at the largest IWC and temperature bins. Combined, this improves the seamless transition across different convective ice hydrometeors (snow and rimed ice) in the model.

Since such a regime where cloud ice particles are smaller than 50 μm is lacking in observations, another scheme should be used to parameterize the terminal velocity of small ice particles (i.e., cloud ice crystals in bulk schemes). Thus, the cloud ice terminal velocity parameterization following the *X-Re* relationship is developed based on the small ice crystal assumption (see Appendix A for derivation information). Hereafter, we refer to this *X-Re* terminal velocity parameterization as the XReICE scheme. For the first time, the *X-Re* relationship is used for representing cloud particle fall speed in a GCM. The factors α and β of the *X-Re*-derived *Vt-D* power-law relationship are also listed in Table 1, and these factors depend on both particle (e.g., mass, size) and air flow (e.g., viscosity) properties. As part of the EL17 field campaign analyses, they found that an *m-D* relationship that best reproduced their results was given by $m = 0.06D^{2.07}$, where m denotes mass in kg and D denotes maximum dimension in meters. We use this *m-D* relationship for cloud ice sedimentation (in Eq. A5, Appendix A), but currently do not propagate it through the rest of the model. This *X-Re*-derived *Vt-D* treatment could be easily extended to cloud ice in stratiform microphysics schemes when an appropriate *m-D* relationship is provided.

Figure 2 shows the *Vt-D* relationships for ice particles (cloud ice, snow and rimed ice particles) at 500 hPa and -5°C. The results at 300 hPa and -35°C show a slightly larger *Vt* due to the less dense air aloft but are very similar to those at lower levels. Here, cloud ice terminal velocity in MG08 (denoted as MG08-ice) (Ikawa and Saito, 1990) is shown for comparison to the XReICE sedimentation scheme (denoted as XReICE-ice). XReICE produces a fall velocity that is a factor of five slower than MG08 across the typical cloud ice size ranges (Figure 2a). Previous studies (Heymsfield et al., 2013; Heymsfield and Westbrook, 2010) suggested that the empirical formulae overestimate terminal velocity for small ice particles because of the particle area ratio consideration and pressure-dependent correction. The agreement between the XReICE sedimentation scheme and the complete *X-Re* terminal velocity parameterization that considers the particle area ratio (Heymsfield and Westbrook, 2010) (denoted as HW10) (Figure 2a) suggests that the mathematical simplifications made for the *X-Re* scheme (see Appendix A) do not jeopardize the accuracy of the results. For convective snow, the EL17 scheme (denoted as EL17-0.05 and EL17-0.5 in Figure 2b) results in substantially larger terminal velocities than the original SZ11 scheme (denoted as SZ11-snow) (Locatelli and Hobbs, 1974) particularly for larger snow particles. For rimed ice hydrometeors, the hail and graupel terminal velocities from Matson and Huggins (1980) and Locatelli and Hobbs (1974), respectively, are also shown in Figure 2c for comparison. The EL17 scheme produces smaller speeds than those by Locatelli and Hobbs (1974) at sizes smaller than ~300 μm. EL17 also produces larger speeds than those by Matson and Huggins (1980) at sizes larger than ~600 μm. Compared to our new terminal velocity parameterizations, the empirical *Vt-D* relationships with constant pre- and exponential factors seem like overestimate the terminal velocity for smaller particles (e.g., cloud ice crystals, small snow and rimed ice particles), and underestimate the terminal velocity for larger particles (e.g., large snow and rimed ice particles). Moreover, the EL17 scheme shows a sensitivity to various ice masses (EL17-0.05 and EL17-0.5), indicating the dependence of fall speeds on particle density to some extent.

Ideally, the other microphysical processes, in particular the collection processes, should fuse the new treatments of the ice particle terminal velocity. The XReICE and EL17 schemes are only used for ice particle sedimentation; thus, consistency across the whole set of microphysical processes is not achieved at present. Future effort is required to couple improved ice particle terminal velocity with other microphysical processes and improve the consistency.

2.2.2 Rimed ice microphysics

Recall that SZ11 is a four-class cloud hydrometeor (cloud droplet, cloud ice, rain and snow) scheme. Riming processes are partly considered in SZ11, while their end product is assigned as snow (e.g., accretion of rain by snow to form snow). Unfortunately, convective snow does not automatically exhibit the characteristics of rimed ice particles. The increase of ice fall speed accompanying with riming (Lin et al., 2011) has not been reflected when the end product is snow in SZ11. Adding rimed ice particles is thus necessary for a more realistic representation of convective microphysical processes. Wu et al. (2013) pointed out that there is more snow in the stratiform region but more rimed ice in the convective region in their study of the impacts of ice processes on simulated squall lines.

A series of microphysical processes associated with rimed ice is added into the SZ11 scheme and is schematically shown in Figure 1 (in blue). The productions of rimed ice hydrometeors are detailed in Appendix B. They include the accretion of cloud droplets by snow to form rimed ice, collection of rain by snow, collection of snow by rain, freezing of rainwater, and accretions of cloud liquid/rainwater by rimed ice. The sink of rimed ice hydrometeors is sedimentation. Note that the accretion of cloud droplets by snow, the accretion of rain by snow, homogeneous and heterogeneous freezing of raindrops were considered in the default SZ11 scheme as source terms for the snow budget. However, now these are adjusted to serve as source terms for both snow and rimed ice budgets when rimed ice microphysics is implemented. In addition, two new processes (i.e., accretion of cloud liquid and rainwater by rimed ice) are introduced.

The gamma distribution, $\phi(D) = N_0 D^{\mu} e^{-\lambda D}$, has been found to fit the observed rimed ice spectra well (e.g., see Figure 1.2 and 1.3 in Straka 2009; Ziegler et al., 1983). This is because rimed ice is usually produced by coalescence of cloud hydrometeors, rather than aerosol activation with follow-up water vapor condensation, implying a negligible amount of rimed ice hydrometeors with sizes close to zero in the size distribution. However, most previous modeling studies (e.g., Gettelman et al., 2019; Ikawa and Saito, 1990; Lin et al., 1983; Reisner et al., 1998) conventionally represented rimed ice spectrum with the inverse-exponential distribution ($\mu = 0$), where the ice particle numbers unwantedly concentrate in small size ranges. Shan et al. (2020) illustrate that a gamma function with nonzero μ can accurately fit the size distribution of particles generated by coalescence. Thus, in this study we use a gamma distribution function with a prescribed shape parameter of μ =3 to represent the rimed ice spectrum. The general microphysical process equations considering the nonzero shape parameter for rimed ice (μ_g) are given in detail in Appendix B. Inclusion of rimed ice also requires changes to the existing water budget equations for the evolution of other hydrometeors and for water budget conservation. These changes are also detailed in Appendix B. The bulk density of rimed ice ρ_g is 500 kg m^{-3} (Gettelman et al., 2019). Terminal velocity of rimed ice hydrometeors is based on EL17 and is shown in Figure 2c. All rimed ice contributes to the convective precipitation. Excluding the detrained snow (see section 2.2.3), the remainder, which refers to as the sedimenting component of snow, contributes to precipitation. Note that cloud ice, rain and snow in SZ11 are represented by inverse-exponential distributions while cloud water is represented by a gamma distribution. Bulk densities of cloud ice and snow are 500 and 100 kg m^{-3}, respectively.

2.2.3 Convective snow detrainment

For the first time, we consider snow detrainment in the modified convective microphysics scheme and investigate its impact on the model simulated cloud and precipitation properties. Snow particles are only treated as precipitating particles in SZ11, where a balance between snow microphysical production and fallout is assumed within one model time step (e.g., 30 min). This assumption may be problematic since snow particles sediment much more slowly than rimed ice particles and raindrops (Luo et al., 2005). Therefore, a portion of the falling snow particles will not reach the ground and thus should be detrained along with the convective cloud ice to feed the stratiform cloud scheme. Detrained snow is calculated as follows: the detrainment rate calculated by the ZM95 scheme multiplies snow mass mixing ratio and number concentration provided by the SZ11 convective microphysics, thus mimicking the calculations for detrained cloud liquid and cloud ice. Note that the detrained snow particles are relatively small because they represent the portion that does not fall fast enough to reach the ground. The detrained convective snow particles are passed into the stratiform cloud microphysics scheme (MG08).

2.3 Model configuration and experiments

Single Column Model (SCM) simulations with high computational efficiency have been widely used as a testbed for model parameterization development and evaluation (Ghan et al., 2000; Liu et al., 2011; Randall et al., 1996). The SCM version of CAM is used in this study with initial and boundary forcing conditions provided from the constrained variational objective analysis (Wang et al., 2009; Xie et al., 2010; Zhang and Lin, 1997; Zhang et al., 2001). The SCM is run with a time step of 20 min and 30 vertical levels over a horizontal domain of 1.9° (latitude) by 2.5° (longitude).

In addition to the CTRL experiment (CAM5.3 and default SZ11), three sensitivity experiments are performed to investigate the roles of changes in terminal velocity, riming, and the detrainment process in the convective microphysics scheme. In XReICE_EL17, the convective snow terminal velocity in CTRL is replaced by the EL17 scheme and cloud ice is further allowed to fall with the terminal velocity calculated by the XReICE scheme. In XReICE_EL17_rime, riming processes and rimed ice hydrometeors are further considered on top of XReICE_EL17. Finally, in Conv_snow_detr, the XReICE_EL17_rime settings are used, additionally with part of convective snow being detrained into the stratiform clouds.

3. Observational data for model evaluations

The U.S. DOE Atmospheric Radiation Measurement (ARM) program Tropical Warm Pool-International Cloud Experiment (TWP-ICE, Mather and Voyles, 2013; May et al., 2008) took place in Darwin, Australia, during the monsoon period in 2006 (January-February) with a focus on gaining a deeper understanding in tropical convective clouds. The Darwin area experiences a wide array of convective systems consisting of active monsoon periods with typical maritime storms and break periods with more coastal and continental convection during TWP-ICE. Our study focuses on the cloud properties observed during the active monsoon period (i.e., 19-25 January 2006) unless otherwise mentioned.

We use convective and stratiform rainfall rates observed by a C-band polarimetric scanning radar located about 30 km northeast of Darwin for our model evaluation. The data processing technique and quality control are described by Varble et al. (2011). Convective and stratiform precipitation is identified based on the fundamentally different radar reflectivity structures following Steiner et al. (1995).

Observational three-dimensional cloud IWC distributions can be found in Wang et al. (2009). This dataset covering the 10°×10° area centered at the Darwin site (-12.43° latitude, 130.89° longitude) with a 16-km resolution are retrieved using both ground-based cloud radar observations and satellite (NOAA-15,-16,-17,-18) high-frequency microwave measurements (Seo and Liu, 2005; 2006) during TWP-ICE. The retrievals are then averaged over the SCM grid domain during the active monsoon period for model comparison.

For the profiles of upper tropospheric IWC, measurements from the Earth Observing System (EOS) Microwave Limb Sounder (MLS) onboard Aura satellite (https://mls.jpl.nasa.gov/) are used. The standard IWC profiles have a useful vertical range extending up to 83 hPa. The vertical resolution is ~3 km, and the horizontal resolution is ~300 km along-track and ~7 km cross-track. The valid IWC range is 0.3-50 mg m^{-3} at 177 hPa and 0.02-50 mg m^{-3} at 83 hPa (Livesey et al., 2017). The pixel-scale upper tropospheric IWC for January and February 2006 is used and averaged over the SCM grid domain for model comparison.

The convective updraft vertical velocity data collected by the dual-frequency radar wind profiler (RWP, 50- and 920-MHz frequencies) near the Darwin site during the 2005-2006 monsoon season (Williams, 2012) provides estimates for the updraft vertical velocity within convection. A fuzzy-logic echo classification (Giangrande et al., 2013; 2016) was developed to segregate convection (including convective cores, convective cloud edges and the associated periphery convective anvils) from stratiform clouds. These observations were documented by Kumar et al. (2015), and we maintain similar concepts by only presenting the statistical properties of convective updrafts from events having at least 5-minutes of continuous convection as flagged by the echo classification.

4. Results

4.1 Terminal Velocity

Terminal velocity of a single cloud hydrometeor is not a quantity directly used in bulk schemes. Instead, the averaged terminal velocity weighted by mass or number is used. Mass-weighted terminal velocity (V_m) is calculated by integrating the cloud hydrometeor terminal velocity over the entire size spectrum weighted by mass mixing ratio. Figure 3 shows vertical profiles of the mass-weighted terminal velocities for cloud ice, snow, and rimed ice particles from the CTRL and Conv_snow_detr simulations. The convective cloud ice V_m from the XReICE sedimentation scheme is ~0.15 m s^{-1}, comprising peaks near 6 and 10 km (Fig. 3a). The new convective snow V_m is significantly smaller between 10-16 km, but larger below 10 km than the CTRL simulation (Figure 3b), indicating a less (more) efficient removal of snow at higher (lower) altitudes. The mass-weighted terminal velocity is expected to increase with the hydrometeor mean diameter that can be expressed as $\frac{1}{\lambda}$ where λ is the slope parameter in the particle size distribution (see Eq. 18 in MG08); namely, the larger the particles are, the faster they fall out. Larger particles are usually detected at lower altitudes due to the growth by collision-coalescence during the precipitation stages (e.g., Stith et al., 2002) as well as due to natural size sorting and sinking of larger particles. Therefore, we argue that the EL17 scheme, with fall speeds peaking at lower altitudes, captures a more realistic vertical distribution of hydrometeor V_m. The terminal velocity of rimed ice particles is derived from the EL17 scheme (i.e., its "denser" ice version), as described earlier. The rimed ice V_m also increases with decreasing altitude and peaks at 6 km with a value of 6 m s^{-1}.

Time-series of observed and modeled total precipitation rates and the break-down of simulated total precipitation to convective and stratiform precipitation in the CTRL simulation are shown in Figures 4a-c. Figures 4d-f show the differences of total, convective and stratiform precipitations between other experiments and CTRL (i.e., other experiments minus CTRL simulation). Intense precipitation was observed from 19 to 25 January, during which the heaviest rainfall occurred on 23 January, followed by a period of light precipitation (Figure 4a). The simulated total precipitation rates are similar among all the simulations, and are in an excellent agreement with observations (within 5% difference; Figure 4 and Table 2). However, previous studies show significant biases in simulated components of convective and stratiform precipitations (Dai, 2006; Qian et al., 2015; Varble et al., 2011), which might partly stem from convective and stratiform cloud microphysics schemes. Stratiform and convective precipitations are directly produced through stratiform and convective microphysics, respectively. Benefiting from rainfall measurements separating the stratiform from the convective precipitation, comparing the precipitation partitioning between model simulations and observations would reveal some insights about the biases of precipitation estimates associated with microphysical schemes.

In Table 2, we provide the observed total, convective, and stratiform precipitation rates (reported as volumetric rainfall rates by Varble et al. (2011) in their Table 3). To compare with model grid-cell mean values, these volumetric rainfall rates are divided by the domain area (i.e., 176×176 km^2) to obtain estimates of domain-mean values. By separating the total precipitation into convective and stratiform components, we find that the majority (62%) of observed total precipitation is contributed by convective precipitation during the active monsoon period (Table 2). In the CTRL simulation, the simulated convective contribution accounts for 64%, whereas the stratiform contribution accounts for 36%.

By modifying convective cloud ice and snow terminal velocities (XReICE_EL17), there is a negligible change in stratiform and convective partitioning (Table 2). Upon addition of rimed ice particles and associated riming processes (XReICE_EL17_rime), the slight increase in convective precipitation is consistent with previous studies (e.g., Wu et al., 2013). In all simulations except Conv_snow_detr, only convective cloud ice and cloud liquid were permitted to detrain into stratiform clouds. In such a case, simulated stratiform precipitation is insensitive to the modifications made in the convective microphysics scheme. When convective snow is allowed to detrain (see section 2.2.3), an increase (decrease) in stratiform (convective) precipitation is noted (Conv_snow_detr versus XReICE_EL17_rime in Table 2). There are two positive spikes in stratiform precipitation between 23 to 25 January (Figure 4f) coincident with two negative spikes in convective precipitation (Figure 4e) when detrainment mainly occurs (see Figure 9). Snow detrainment “seeds” stratiform clouds and “feeds” cloud liquid droplets, thus boosting stratiform precipitation. It is worth noting that model estimates are all within observational uncertainty bounds (Table 2). Continual evaluation and improvement of convective and stratiform cloud microphysics, along with a reduction in observational uncertainty, will allow for an assessment of the true biases in the precipitation simulation(s).

We define the frozen water content (FWC) as the sum of cloud ice and snow (and rimed ice where applicable). Figure 5 shows observed and simulated vertical distributions of grid-mean total FWC (i.e., convective FWC + stratiform FWC) averaged over the active monsoon period. Note that simulated cloud ice and precipitating ice (i.e., snow and rimed ice) masses were combined because observations cannot robustly distinguish between them. Observed FWC profile shows a maximum of 120 mg m^{-3} at about 8 km, and more broadly, high FWC values exceeding 100 mg m^{-3} extend from 6 to 8 km. The CTRL run captures the shape of observed FWC profile but systematically overestimates the FWC. Relative to observations, the CTRL simulation overestimates the total FWC by 73% at ~8 km and by more than 100% above 10 km. We can divide the whole FWC profile into three parts: melting layer (i.e., 3 km to 6 km), mixed-phase layer (i.e., 6 km to 10 km) and cold-phase layer (i.e., above 10 km). Observations within the mixed-phase and melting layers are more uncertain because of the co-existence of supercooled liquid droplets and solid ice particles. The model overestimation of total FWC below 6 km is likely related to the stratiform counterpart (Figure 6), and/or the satellite estimates may be biased low since satellite instruments cannot detect cloud hydrometeors within the lower parts of precipitating deep convective systems due to microwave signal attenuation in rain and graupel. Therefore, we mainly focus on the simulated FWC at the cold-phase layer and qualitatively evaluate the simulated FWC below. In the tropical region, the 10 km layer usually corresponds to the -37 ℃ isotherm layer where the homogeneous freezing of cloud and rain droplets generally occurs, and all hydrometeors are in the solid phase. Figure 6 shows the time-height cross sections of convective (left) and stratiform (right) FWC. In the CTRL simulation, convective FWC dominates above 6 km, suggesting most of the overestimated FWC when compared with observations in Figure 5 is because of the convective counterpart. As a result, the high FWC bias should be attributed partly to the underestimated falling speed of ice particles. Further note that snow particles dominate the solid particle mass, suggesting that the underestimated snow particle terminal velocity might be one of the bias sources.

The simulated total FWC in the XReICE_EL17 run is decreased by ~25% (~23%) at 12 km (10 km) relative to the CTRL simulation and is in better agreement with observations (Figure 5). XReICE_EL17 introduces more effective sedimentation of solid particles by increasing snow particle falling speed and enabling cloud ice crystal sedimentation, which partially removes high FWC bias in particular above 10 km (also see Figure 6c). Note that XReICE_EL17 still overestimates total FWC by 50% (25%) at 12 km (10 km) when compared with observations. Improving the convective cloud ice and snow sedimentation is not sufficient to correct the vertical distribution of FWC in the mid- and upper-troposphere. This is because the bulk convective microphysics with snow as the only precipitating ice particles would "underestimate" the solid particle terminal velocity because it does not account for the effects of faster-falling rimed ice particles. The results in Figure 5 indicate that upon consideration of the dense rimed ice particles (XReICE_EL17_rime), the vertical distribution of FWC is further improved and agrees well with observations above ~10 km. Consideration of rimed ice hydrometeors denser than snow particles is an effective approach for further increasing the solid particle sedimentation (Figure 3c) and eliminating the high FWC bias (Figure 6e). In Conv_snow_detr, a portion of convective snow particles is detrained into stratiform clouds where they sediment at the speed of stratiform cloud particles, rather than being converted into rimed ice in the convective clouds. The stratiform FWCs show detectable increase in the upper troposphere on 23rd January when detrainment mainly occurs (see next section). Consequently, Conv_snow_detr simulates slightly higher FWC than XReICE_EL17_rime, but still shows large improvements in the simulated FWC profile over the CTRL simulation (Figure 5).

Regarding the upper tropospheric FWC (Figure 7), MLS observations show FWCs ranging from ~10 mg m^{-3} at 140 hPa to ~30 mg m^{-3} at 180 hPa. The simulated FWCs in the CTRL simulation are about 2 times of the MLS values at these altitudes. Improving the convective ice particle fall speeds reduces the bias in the simulated upper tropospheric FWC (Figure 7). Including rimed ice particles further improves the simulated FWCs. Upon considering snow detrainment, the simulated FWC vertical distribution also agrees well with observations. The MLS IWC retrievals are considered to be reliable in this study because it is comparable to an independent three-dimensional IWC observational product (Seo and Liu, 2005) (see our Figure 5 above 12 km).

In summary, applying new convective ice particle terminal velocity parameterizations along with added dense rimed ice particles greatly improves the vertical structure of simulated convective cloud condensate.

4.2 Detrainment

It is well established that ice detrainment from deep convection is a critical source for the generation of upper tropospheric stratiform anvil clouds over the tropics (Biggerstaff and Houze, 1991; Gamache and Houze, 1983; Rutledge and Houze, 1987; Smull and Houze, 1985; Fu et al., 1995; Krueger et al., 1995; Zeng et al., 2013). Currently in CAM5.3 with SZ11, detrainment is parameterized by the product of the rate at which cloud condensate detrains and the amount of cloud condensates. The complex and multiple physical processes responsible for detrainment are often described in a single parameter: detrainment rate. Unfortunately, a lack of available observations hinders an efficient verification of the use of the detrainment rate. On the other hand, noting the improvement in convective microphysical properties in terms of vertical profiles of FWC (section 4.1), it is a natural next step to investigate the connection between convective and stratiform clouds through detrainment. In a modeling study using the SZ11 convective microphysics scheme, Storer et al. (2015) pointed out that deep convection is too active, and detrainment might be insufficient in the CAM model.

The detrained ice mass mixing ratio and number concentration with and without snow detrainment are shown in Figures 8 and 9. The profile of detrained ice mass in the XReICE_EL17_rime simulation exhibits a bimodal distribution, with peak values of ~15 mg m^{-3} at 8 and 15 km. The upper-peak (associated with the deep convection) is comparable in magnitude with the lower-peak (corresponding to congestus or detrainment from the lower part of deep cores). With the addition of snow detrainment (Conv_snow_detr), the detrained ice mass profile retains the apparent bimodal distribution, and the magnitude increases consistently up to 16 km. The two peak values become ~25 and 45 mg m^{-3} at 8 and 15 km, respectively. One striking feature is the marked increase in the detrained mass above 10 km relative to the XReICE_EL17_rime simulation. The range of mass detrainment heights (from 8 km to 15 km) for deep convection is comparable to previous findings informed by analysis of satellite and ground-based observations over the ARM TWP Darwin site (Deng et al., 2016; Takahashi et al., 2017; Wang et al., 2020). Though quantifying and deriving detrained ice requires further novel observational techniques and modeling studies, inclusion of snow detrainment does alleviate a suspected underestimation of detrained FWC (Figure 8a).

The number concentration of detrained ice particles in the XReICE_EL17_rime simulation (Figure 8b) displays a peak value of ~0.3 cm^{-3} near 15 km. With the addition of snow detrainment in the Conv_snow_detr simulation, detrained ice number concentration (sum of cloud ice and snow number concentration, although cloud ice number concentration is dominant) displays a peak value of ~0.25 cm^{-3} at about 14 km and it decreases above 14 km but increases below 14 km relative to the results of XReICE_EL17_rime.

The detrained ice mass and number in the time-height cross-sections (Figure 9), on average, increase consistently in every convective event when snow detrainment occurs in the Conv_snow_detr simulation (Figure 9c-d). We note that detrainment occurs in deep layers spanning several kilometers and is not confined within a thin layer near cloud top. This is suggested as more realistic and consistent with cloud-resolving model and large-eddy simulation results (Luo et al., 2005). Furthermore, detrainment occurs at different altitudes corresponding to clouds with various vertical extents. In general, there are no significant changes in the vertical and temporal structures of detrained mass between XReICE_EL17_rime and Conv_snow_detr except in magnitude.

The Multifunctional Transport Satellite (MTSAT) provides the observational outgoing longwave radiation (OLR), with data derived from use of the visible infrared solar-infrared split window technique (Minnis et al., 2002). The top of the atmosphere (TOA) OLR is closely related to ice cloud properties in the upper troposphere. As a result, we might expect impacts on OLR due to the combined changes in Conv_snow_detr. The OLR is mostly overestimated in the CTRL and Conv_snow_detr simulations (Figure 10), indicating more longwave radiation is escaping than is observed, resulting from potential biases in simulated cloud amount and/or cloud top height (temperature). However, the difference of simulated OLR between CTRL and Conv_snow_detr simulations is noted when detrainment occurs (i.e., January 23rd). In the Conv_snow_detr simulation, the simulated OLR is much improved on January 23rd. Despite a significant amount of IWC detrainment, the increase of upper tropospheric ice clouds is small, which is more constrained by the large-scale forcing data.

The decrease in OLR is thus likely related to increase in cloud top IWC and/or higher cloud top height. Before January 23rd when there is no significant detrainment occurring, the overestimation of OLR reveals systematic errors in the model. On the second half of the January 24th, the underestimation of OLR is slightly degraded in the Conv_snow_detr.

Figure 11 shows the time-pressure cross-sections of temperature and specific humidity differences between (a, b) CTRL and observations, (c, d) XReICE_EL17 and CTRL, (e, f) XReICE_EL17_rime and CTRL, and (g, h) Conv_snow_detr and CTRL. The temperature and specific humidity from the TWP-ICE forcing data are used for simulation evaluation. The CTRL simulation shows cold biases mostly in the middle troposphere and dry biases throughout the troposphere. Dry biases are found in particular below 600 hPa during the active monsoon period, which is consistent with the findings in Song and Zhang (2011, see their Figures 5 and 6). It is identified that the dry bias on 23-24 January is mainly induced by the strong drying effect of deep convection. The cold bias may be attributed in part to the simulated overestimation of OLR.

Compared to the CTRL simulation, the large-scale heat and moisture fields in the other experiments are somewhat improved in some regions but become worse in others. For example, the temperature becomes warmer at about 600-400 hPa on 22 January and at ~600 hPa from the second-half day of 23 January to 25 January, but becomes cooler between 800 and 600 hPa on 22 January and between 800 and 700 hPa on 23 January in the Conv_snow_detr simulation than the CTRL simulation (Figure 11g); the atmosphere becomes mostly wetter at about 600 hPa during 23 to the first-half day of 24 January, yet becomes largely drier between 800 and 600 hPa on 22 January and at 800 hPa during 23-24 January in the Conv_snow_detr simulation than the CTRL simulation (Figure 11h). Most of the temperature changes in the sensitivity simulations compared to the CTRL simulation are due to the changes in evaporative cooling and convective heating in the ZM95 scheme, and to a lesser extent in longwave cooling and shortwave warming. The increase in specific humidity below 800 hPa in the XReICE_EL17 simulation (Figure 11d) and below 600 hPa in the XReICE_EL17_rime simulation (Figure 11f) relative to the CTRL simulation can be caused by the enhanced precipitation evaporation in light of the enhanced precipitation rate (Table 2). An increase in detrainment results in moistening of the atmosphere, as well as enhanced anvil clouds that have warming effects (Fu et al., 1995) which may explain the increase in moisture and temperature seen in the middle and upper troposphere in the Conv_snow_detr simulation on 23 January (Figure 11g and 11h).

It is noted that the changes made in the convective microphysics scheme modify the microphysical and radiative behavior of convective clouds, leading to changes in their role in redistributing heat and moisture in the environment. All subsequent changes are difficult to explicitly explain by a single physical process due to the complex and non-linear interaction between convective and stratiform clouds.

4.3 Updraft velocity

An analysis of simulated convective updraft velocity may also provide insights into the overestimation of simulated total FWC in the CTRL run in addition to cloud hydrometeor terminal velocity. Among many microphysical processes, the ice deposition that depends on supersaturation is the dominant term for ice mass production. Water vapor supersaturation scales with convective updraft vertical velocity that can thus be considered as a proxy for the FWC source. In SZ11, the convective updraft velocity is calculated using the kinetic energy budget equation that is adopted from the European Center for Medium-range Weather

Forecast (ECMWF) model. New vertical velocity retrievals for deep convective clouds developed using Radar Wind Profiler (RWP) observations (e.g., Williams 2012; Giangrande et al., 2013; 2016; Kumar et al., 2015; Wang et al., 2019) enable an evaluation of simulated updraft properties against observations.

RWP retrieved and model simulated cumulative frequency by altitude diagrams (CFADs) (Yuter and Houze, 1995) are shown in Figure 12. Comparing model simulations and RWP observations can be difficult because the model outputs represent temporal and spatial averages, whereas the RWP measurements represent an 'instantaneous' estimate for a relatively small illuminated radar volume O[1km]. One of the advantages of using CFADs is that the normalized frequency from the observations is less sensitive to the spatial scale, which to some extent relieves the difficulties in comparing GCM simulations with instantaneous point observations. Retrieved updraft properties are available from the 2005-2006 monsoonal period, and updraft vertical velocities are processed only when convection is identified (see section 3). The sample size for these retrievals includes data from ~40 separate convective event/days. The associated CFAD reflects ~113,000 instantaneous profiler estimates of the convective updraft vertical velocity at all altitudes with ~1,000 samples at almost each altitude. Note, the sample size from our simulations is ~420 convective events during TWP-ICE, where we define the number of convective events as the numbers of convective microphysics triggered. The associated CFAD shows ~5,000 simulated convective updraft vertical velocity outputs at all height levels with ~40 (~400) samples at higher (lower) altitudes. The CFAD bin size is 0.5 m s^{-1}.

The observed convective updraft vertical velocity (Figure 12a) exhibits large variability, with frequent and intense updraft velocities, as well as numerous profiles with speeds less < 1 m s^{-1}. This is common in the observations, as we often sample the updraft cores as well as the periphery regions and transitions to downdraft conditions at the edges of the more intense updraft regions. The model simulations (Figures 12b, c, and d) yield profiles clustered between the two extremes, particularly at altitudes higher than 6 km. Few simulated updraft velocities reach 12 m s^{-1} above 7 km in the CTRL simulation (Figure 12b) while the Conv_snow_detr simulation tends to simulate some larger velocities at higher altitudes (Figure 12c). It is noted that simulated maximum velocities do not exceed 15 m s^{-1} (Figures 12b and c) since an upper bound of 15 m s^{-1} is set to the convective updraft vertical velocity in SZ11. Meanwhile, observed maximum values exceed 15 m s^{-1} at almost all altitudes (instantaneous extreme event samples). Removing the 15 m s^{-1} upper bound threshold allows the model to simulate some updraft velocities larger than 15 m s^{-1} between 4-8 km (Figure 12d). We also increase the simulated convective updraft velocities by a factor of two (Figure 12e) for sensitivity test purpose, leading to a significant increase in simulated FWC (not shown). We also perform a sensitivity test by replacing the ECMWF scheme with the Gregory (2001) scheme for convective updraft velocity calculations. This scheme allows the model to reproduce the strong updrafts at higher altitudes after removing the 15 m s^{-1} upper bound (Figure 12f). The normalized sampling number from simulations is comparable to that from observations (not shown). It is thus implied that the parameterization for convective updrafts outweighs sampling issues because the Gregory scheme is able to simulate strong updrafts at higher altitudes given the similar sampling numbers from model simulations. Detailed analyses of the structure and impact of both parameterizations are beyond the scope of this work.

At the low end of the updraft velocity spectrum, we find that the model fails to reproduce the weaker updraft vertical velocities seen in the observations. At every altitude, the observations suggest that weak (< 5 m s^{-1}) updraft velocities are common, followed by a gradual decrease in the frequency of updrafts occupying higher velocity bins. In the model, simulations often produce moderate updraft velocities extending from ~3 to ~10 m s^{-1}, with fewer occurrences of low and high velocities. A number of these differences can be partially explained by the effects of spatial averaging. The convective edges and periphery convection are included in the updraft velocity retrievals, and these regions typically have lower velocities. On the other hand, the simulated convective updrafts are at sub-grid scale and are assumed homogeneously uniform in convection, and as such, the lower velocities associated with peripheries would not be captured. The absence of the heterogeneity also implies that simulated updrafts would miss the most intense inner core of a convective updraft, and therefore, significant underestimation of the occurrence frequency of strong convective updraft vertical velocities is also expected. Finally, what increases the difficulty in comparing simulated bulk convective updrafts with observations is the concept of bulk or ensemble in the current convection scheme used in GCMs. To reduce computational cost, cumulus plumes with different intensity and depth are averaged over the whole cumulus spectrum. In contrast, observed convective updrafts are obtained from individual convective instances. To better represent updraft vertical velocity in the model, a spectral or probability density distribution accounting for the heterogeneity should be used to better represent the real nature of convective systems.

The lack of variability in updraft velocities plausibly has a large impact on the microphysical processes such as cloud droplet activation and ice nucleation. Homogeneous aerosol freezing and heterogeneous ice nucleation are parameterized to occur in weak updrafts (< 4 m s^{-1}), while homogeneous droplet freezing is parameterized to occur in strong updrafts following Phillips et al. (2007) in the SZ scheme (Song et al., 2012). The absence of both weak and strong updrafts leads to the suppressed ice nucleation and droplet freezing, and combined with a dry bias in the model (Figure 11), a low bias in the production of cloud ice is likely expected.

5. Summary and Conclusions

This study implements four improvements to the SZ11 convective microphysical parameterization in NCAR CAM5.3. They include (1) incorporation of cloud ice particle fall velocities; a universal dependence of *Vt* on particle and air flow properties formulated in terms of *Davis* or *Best* (*X*) and *Reynolds* (*Re*) numbers (in the form of power-law relationships) has been developed (see detailed mathematical derivations in Appendix A) and is used for the first time in atmospheric models, (2) replacement of the snow terminal velocity formulation with a more adequate parameterization for convective snow, (3) addition of a rimed ice hydrometeor category to the SZ11 existing four classes (cloud liquid, cloud ice, rain, and snow), and (4) the enabling of convective snow particles to be detrained. This work improves the physical basis for the removal of cloud condensates in a convective microphysics scheme and complements the work that includes rimed ice hydrometeors in a stratiform microphysics scheme (Gettelman et al., 2019).

The simulated total FWC from the CTRL run is overestimated by 73% at 8 km and more than 100% above 10 km compared to the observation averaged over the active monsoon period. By looking into the convective and stratiform counterparts, it is found that most of the FWC above 6 km is largely contributed by convective clouds. The parameterization in

SZ11 tends to underestimate the terminal velocity of ice particles in convection, leading to an underestimation in the removal of cloud and precipitating particles. By implementing a convective-oriented ice particle terminal velocity parameterization (i.e., the EL17 scheme) for snow, and enabling convective cloud ice to fallout, the total simulated FWC in XReICE_EL17 is decreased and becomes closer to observations. However, XReICE_EL17 still overestimates total FWC by 50% at 12 km and 25% at 10 km when compared with observations. After adding the dense rimed ice particles into the convective microphysics scheme, the vertical distribution of FWC is further improved and exhibits the best agreement with observations above ~10 km. Therefore, the underestimation of ice particle terminal velocity, likely implying an underestimated sink of cloud and precipitating condensates, plays an important role in the overestimation of simulated FWC.

The detrained ice mass mixing ratio and number concentration are investigated. There is a marked increase in detrained ice particle mass above 10 km along with an increase in detrained ice particle number with the addition of snow detrainment. The simulated OLR is improved with snow detrainment when detrainment mainly occurs (January 23rd).

We also examine the simulated convective updraft vertical velocity. Relative to RWP retrievals, we find that the model significantly underestimates the occurrence frequency of both strong and weak convective updraft vertical velocities.

The simulated microphysical properties of detrainment from models need to be evaluated against observations in the future; such an analysis will be important for constraining and reducing the uncertainties associated with anvil clouds. Impacts of the inclusion of snow detrainment on climate (e.g., water and radiative energy budgets in the upper troposphere and general circulation) should also be investigated. It is important that convective cloud microphysical properties are simultaneously analyzed with convective updraft vertical velocities since all such variables are coupled, ensuring that they are all correct so that model simulations and climate projections are improved for the right reasons.

Appendix A – *Davis-Reynolds number V_t parameterization*

Previous studies (Abraham, 1970; Beard, 1980; Böhm, 1989; 1992) have established an analytical expression to relate the *Davis* or *Best* number (*X*) and *Reynolds* (*Re*) number as follows:

$$X \equiv C_D Re^2 = \frac{\rho_a 2mgD^2}{\eta^2 A} \tag{A1}$$

where C_D is the drag coefficient, g is the gravitational acceleration in m s^{-2}, η is the air dynamic viscosity as a function of temperature in poise with an accuracy of $\pm 0.002 \times 10^{-4}$ poise (Pruppacher and Klett, 1997, pp.417), ρ_a is the air density in kg m^{-3}, *m* denotes the mass of individual ice particle in kg ($m = aD^b$), and *A* denotes the cross-sectional area of individual particles in m^2 ($A = \gamma D^\sigma$). *D* is particle maximum dimension. After further substitution of the drag coefficient as a function of *Re*, $C_D = C_0\left(1 + \delta_0/Re^{1/2}\right)^2$(Abraham, 1970), we get a *X*-*Re* relation:

$$Re = \frac{\delta_0^2}{4}\left[\left(1 + \frac{4\sqrt{X}}{\delta_0^2\sqrt{C_0}}\right)^{1/2} - 1\right]^2 \tag{A2}$$

where $C_0 = 0.35$, and $\delta_0 = 8.0$ (Heymsfield and Westbrook, 2010). The terminal velocity of individual cloud particles for a given environmental condition is calculated as follows:

$$v_t = \frac{\eta Re}{\rho_a D} \tag{A3}$$

Eliminating *X* and *Re* by combining Eqs. (A1), (A2) and (A3), we get

$$v_t = \frac{\eta}{\rho_a D}\frac{\delta_0^2}{4}\left[(1+f(D))^{1/2}-1\right]^2 \tag{A4}$$

$$\mathrm{f(D)} = \frac{4}{\delta_0^2\sqrt{C_0}}\left[\frac{\rho_a 2mgD^2}{\eta^2 A}\right]^{1/2} = \frac{4}{\delta_0^2\sqrt{C_0}}\left[\frac{\rho_a 8mg}{\eta^2 \pi A_r}\right]^{1/2} \tag{A5}$$

when the area ratio $A_r = A/[(\frac{\pi}{4})D^2]$ of a particle is introduced into $\mathrm{f(D)}$. It is not straightforward to analytically solve the integration of v_t in Eq. (A4) over the entire size spectrum due to the complex function of *D* (Note that *m* and *A* is also a function of *D* within the square root). This *X-Re* based ice particle terminal velocity relationship has been primarily informed through laboratory experiments (e.g., Heymsfield and Westbrook, 2010), and it also serves as a benchmark for validating the empirical *Vt-D* power-laws (e.g., Mitchell, 1996). However, the complete *X-Re* terminal velocity parameterization is seldom used in atmospheric modeling because its complexity of the algebraic equations makes it difficult to obtain an analytical expression for use in bulk microphysics schemes. A further simplification is made to obtain a power-law relationship to facilitate use in bulk schemes.

By setting $\mathrm{Z(D)} \equiv \frac{4\sqrt{X}}{\delta_0^2\sqrt{C_0}}$, we get:

$$Re = \frac{\delta_0^2}{4}\left[(1+Z)^{1/2}-1\right]^2 \approx \frac{\delta_0^2}{4}\left[\frac{Z}{2}\right]^2 \tag{A6}$$

Here it is assumed that *Z* is much smaller than unity. Reynolds number Re can thus be simplified to $Re = X/(\delta_0^2 C_0)$. Substituting the simplified Re into Eq. (A3), v_t can be simplified as:

$$v_t = \frac{2ag}{\delta_0^2 C_0 \eta\, \gamma} D^{b-\sigma+1} = \frac{8ag}{\delta_0^2 C_0 \eta \pi A_r} D^{b-1} \tag{A7}$$

Now v_t is analytically integrable over the whole size spectrum to calculate the mass- and number-weighted terminal velocity. Equation (A7) is valid when *Z* is much smaller than unity. Figure A1 shows that when ice particle dimensions are smaller than 500 μm, *Z* is far smaller than unity across a broad range of temperature and pressure. This study uses v_t in Eq. (A7) to represent the terminal velocity-diameter power-law relationship for cloud ice particles. We assume the area ratio A_r to be unity for simplicity.

The mass-weighted (V_{mi}) and number-weighted (V_{ni}) terminal velocities are calculated as:

$$V_{mi} = \frac{8ag}{\delta_0^2 C_0 \eta\, \pi} \frac{\Gamma(2b)}{\Gamma(b+1)} \lambda^{1-b} \tag{A8}$$

$$V_{ni} = \frac{8ag}{\delta_0^2 C_0 \eta\, \pi} \Gamma(b) \lambda^{1-b} \tag{A9}$$

The above two equations match those in Khvorostyanov and Curry (2002) (their Eqs. 2.14-2.15 for the $X \ll X_{sc}$ regime).

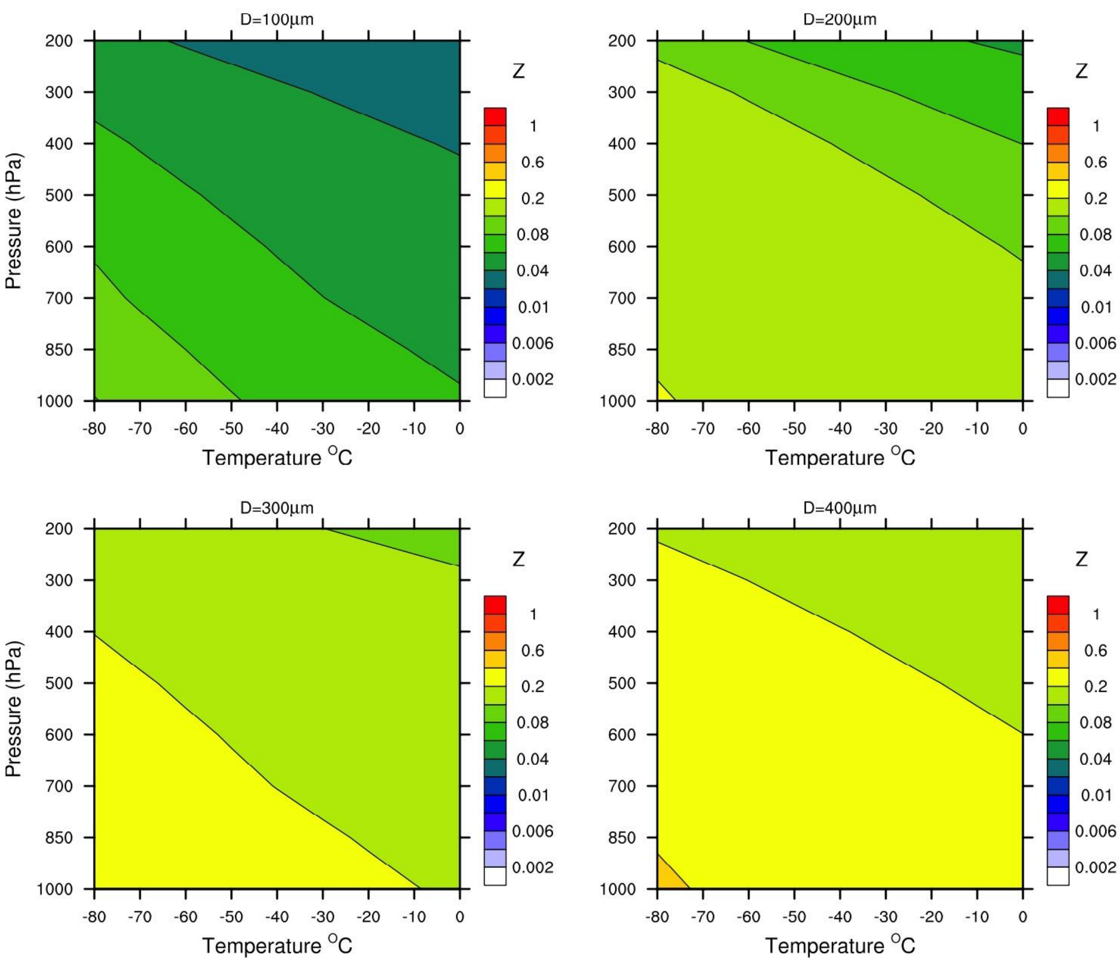

Fig A1. *Z* values as a function of temperature and pressure for different ice particle dimensions.

Appendix B – *Description of the improved convective microphysics scheme*

An equation set including the rimed ice microphysics is given in section (a) for completeness. Detailed process rates for rimed ice microphysics are given in section (b).

(a) Microphysics budget equations

The budget equations for cloud hydrometer mass mixing ratio (q_x in kg kg^{-1}) and number concentration (N_x in # kg^{-1}), where x corresponds to cloud water (c), rain (r), cloud ice (i), snow (s) and rimed ice (g), respectively, are written as follows:

$$\frac{\partial}{\partial z}(M_u q_x) = -D_u q_x + \sigma_u S_x^q \quad \text{(a1)}$$

$$\frac{\partial}{\partial z}(M_u N_x) = -D_u N_x + \sigma_u S_x^N \quad \text{(a2)}$$

where *z* is height; M_u, D_u are the convective updraft mass flux and detrainment rate, respectively, given by the ZM95 scheme, and σ_u is the fractional area occupied by convective updrafts. S_x^q and S_x^N are source/sink terms for q_x and N_x of different hydrometeor species and are written as

$$S_c^q = P_{c.cond}^{qc} - P_{c.auto}^{qc} - P_{racw}^{qc} - P_{c.frz\_hom}^{qc} - P_{c.frz\_het}^{qc} - P_{Berg}^{qc} - P_{sacw}^{qc} - P_{g.gacw}^{qc} \quad \text{(a3)}$$

$$S_c^N = P_{c.act}^{Nc} - P_{c.auto}^{Nc} - P_{racw}^{Nc} - P_{c.frz\_hom}^{Nc} - P_{c.frz\_het}^{Nc} - P_{Berg}^{Nc} - P_{sacw}^{Nc} - P_{g.gacw}^{Nc} \quad \text{(a4)}$$

$$S_r^q = P_{c.auto}^{qc} + P_{racw}^{qc} - P_{r.fallout}^{qr} - P_{sacr}^{qr} - P_{r.frz\_hom}^{qr} - P_{r.frz\_het}^{qr} - P_{g.gacr}^{qr} \quad \text{(a5)}$$

$$S_r^N = P_{c.auto}^{Nc} - P_{r.fallout}^{Nr} - P_{r.agg}^{Nr} - P_{sacr}^{Nr} - P_{r.frz\_hom}^{Nr} - P_{r.frz\_het}^{Nr} - P_{g.gacr}^{Nr} \quad \text{(a6)}$$

$$S_i^q = P_{i.dep}^{qi} + P_{c.frz\_hom}^{qc} + P_{c.frz\_het}^{qc} + P_{Berg}^{qc} - P_{i.auto}^{qi} - P_{saci}^{qi} - P_{i.fallout}^{qi} \quad \text{(a7)}$$

$$S_i^N = P_{i.nul}^{Ni} + P_{c.frz\_hom}^{Nc} + P_{c.frz\_het}^{Nc} - P_{i.auto}^{Ni} - P_{saci}^{Ni} - P_{i.fallout}^{Ni} \quad \text{(a8)}$$

$$S_s^q = P_{i.auto}^{qi} + P_{saci}^{qi} + P_{sacw}^{qc} + P_{sacr}^{qr} - P_{s.fallout}^{qs} - P_{g.sacw}^{qs} - P_{g.sacr}^{qs} - P_{scng}^{qs} - P_{g.racs}^{qs} \quad \text{(a9)}$$

$$S_s^N = P_{i.auto}^{Ni} - P_{s.agg}^{Ns} - P_{s.fallout}^{Ns} - P_{g.sacw}^{Ns} - P_{g.sacr}^{Ns} \quad \text{(a10)}$$

$$S_g^q = P_{g.sacw}^{qs} + P_{scng}^{qs} + P_{g.sacr}^{qs} + P_{g.racs}^{qs} + P_{r.frz\_hom}^{qr} + P_{r.frz\_het}^{qr} + P_{g.gacw}^{qc} + P_{g.gacr}^{qr} - P_{g.fallout}^{qg}$$

(a11)

$$S_g^N = P_{g.sacw}^{Ns} + P_{g.sacr}^{Ns} + P_{r.frz\_hom}^{Nr} + P_{r.frz\_het}^{Nr} - P_{g.fallout}^{Ng} \quad \text{(a12)}$$

The source terms of rimed ice hydrometeor include (1) conversion of accretion of cloud liquid by snow to rimed ice ($P_{g.sacw}$), (2) accretion of rain by snow ($P_{g.sacr}$), (3) collection of snow by rain ($P_{g.racs}$), (4) homogeneous and (5) heterogeneous freezing of rain water ($P_{r.frz\_hom}$ and $P_{r.frz\_het}$), and (6)-(7) accretion of rimed ice with cloud liquid/rain water ($P_{g.gacw}/P_{g.gacr}$). The sink term for rimed ice hydrometeors is sedimentation ($P_{g.fallout}$). Note that the accretion of cloud liquid by snow (P_{sacw}), the accretion of rain by snow (P_{sacr}), and homogeneous and heterogeneous freezing of raindrops ($P_{r.frz\_hom}^{qr}$, $P_{r.frz\_het}^{qr}$) are already considered in the default SZ11 scheme as source terms in the snow budget equation but are now adjusted to serve as source terms for the snow and rimed ice budget equations. Modifications have been accordingly applied to the snow budget equation. For instance, a part of the collected cloud water by snow (P_{sacw}^{qc}) now contributes to the production of rimed ice ($P_{g.sacw}^{qs}$) and the remainder contributes to the production of snow itself ($P_{sacw}^{qc} - P_{g.sacw}^{qs}$). Additionally, two new processes (i.e., accretion of cloud liquid $P_{g.gacw}$ and rainwater $P_{g.gacr}$ by rimed ice) neglected in the default SZ11 scheme are introduced into the model. The modifications have also been applied to the cloud liquid and rain mass mixing ratio and number concentration budget equations. Rimed ice increases by collecting cloud ice and snow is not currently included in this work because the collection efficiency between two solid species is small and riming (e.g., the accretion by rimed ice of rain and cloud liquid) is the dominant process for rimed ice formation and growth. Collisions between rain and cloud ice, between cloud liquid and cloud ice, and self-collection of cloud ice are neglected for simplicity.

Rimed ice has been represented by the inverse exponential distribution ($\mu = 0$) in most previous modeling studies (e.g., Gettelman et al., 2019; Ikawa and Saito, 1990; Lin et al., 1983; Reisner et al., 1998), we use a prescribed non-zero shape parameter μ_g of 3 in this study. The general form of the spectral slope and intercept parameters λ_g and N_{0g} derived from q_g and N_g are as follows:

$$\lambda_g = \left[\frac{a_{mg} N_g \Gamma(b_{mg} + \mu_g + 1)}{q_g \Gamma(\mu_g + 1)}\right]^{1/b_{mg}} \quad \text{(a13)}$$

$$N_{0g} = \frac{N_g \lambda_g^{\mu_g + 1}}{\Gamma(\mu_g + 1)} \quad \text{(a14)}$$

a_{mg} and b_{mg} are the parameters in the mass-diameter power-law relationship $\mathrm{M}(D_g) = a_{mg} D^{b_{mg}} \rho_g$. Following Morrison et al. (2009), upper and lower bounds for the slope parameter λ_g are specified so that the mean hydrometer diameter cannot be larger than 2000 or smaller than 20 μm for rimed ice. λ_g is prevented from exceeding these bounds by adjusting the number concentration in Eq. (a13). The rest of the scheme, where it is not directly related to rimed ice microphysics, remains the same as the default SZ11 scheme unless further specified.

Mass mixing ratio and number concentration budget equations for cloud liquid, cloud ice, rain and snow from the default SZ11 scheme are given in Appendix C. Readers are recommended to compare the new budget equations [i.e., Eq. a(3)-a(12)] with the default ones [i.e., Eq. c(1)-c(8)] (without rimed ice microphysics).

(b) Production terms for rimed ice

The general continuous collection growth equations, where the collector (species x, subscript x) and collected particle (species y, subscript y) size spectra are represented by gamma distribution function, are given by:

$$P_{xacy}^{qy} = \frac{1}{\rho_a}\int_0^\infty\int_0^\infty \frac{\pi\left(D_x + D_y\right)^2\left(V_{tx} - V_{ty}\right)\left(\frac{\rho_0}{\rho_a}\right)^{\frac{1}{2}} M\left(D_y\right)E_{xy}N_{Tx}N_{Ty}}{4\Gamma(\mu_x+1)\Gamma\left(\mu_y+1\right)}$$

$$\times \lambda_x^{\mu_x+1}\lambda_y^{\mu_y+1}D_x^{\mu_x}D_y^{\mu_y}\exp(-\lambda_x D_x)\exp(-\lambda_y D_y)dD_x dD_y$$

$$= \frac{\pi}{4}a_{my}E_{xy}N_{0x}N_{0y}\Delta\overline{V_m}\left(\frac{\rho_0}{\rho_a}\right)^{\frac{1}{2}}\frac{\rho_y}{\rho_a}\left[\frac{\Gamma(3+\mu_x)\Gamma(1+\mu_y+b_{my})}{\lambda_x^{3+\mu_x}\lambda_y^{1+\mu_y+b_{my}}} + \frac{2\Gamma(2+\mu_x)\Gamma(2+\mu_y+b_{my})}{\lambda_x^{2+\mu_x}\lambda_y^{2+\mu_y+b_{my}}} + \frac{\Gamma(1+\mu_x)\Gamma(3+\mu_y+b_{my})}{\lambda_x^{1+\mu_x}\lambda_y^{3+\mu_y+b_{my}}}\right] \quad \text{(b1)}$$

$$P_{\mathrm{xacy}}^{Ny} = \int_0^\infty\int_0^\infty \frac{\pi\left(D_x + D_y\right)^2\left(V_{tx} - V_{ty}\right)\left(\frac{\rho_0}{\rho_a}\right)^{\frac{1}{2}} E_{xy}N_{Tx}N_{Ty}}{4\Gamma(\mu_x+1)\Gamma\left(\mu_y+1\right)}$$

$$\times \lambda_x^{\mu_x+1}\lambda_y^{\mu_y+1}D_x^{\mu_x}D_y^{\mu_y}\exp(-\lambda_x D_x)\exp(-\lambda_y D_y)dD_x dD_y$$

$$= \frac{\pi}{4}E_{xy}N_{0x}N_{0y}\Delta\overline{V_n}\left(\frac{\rho_0}{\rho_a}\right)^{\frac{1}{2}}\left[\frac{\Gamma(3+\mu_x)\Gamma(1+\mu_y)}{\lambda_x^{3+\mu_x}\lambda_y^{1+\mu_y}} + \frac{2\Gamma(2+\mu_x)\Gamma(2+\mu_y)}{\lambda_x^{2+\mu_x}\lambda_y^{2+\mu_y}} + \frac{\Gamma(1+\mu_x)\Gamma(3+\mu_y)}{\lambda_x^{1+\mu_x}\lambda_y^{3+\mu_y}}\right] \quad \text{(b2)}$$

P_{xacy}^{qy}, P_{xacy}^{Ny} are the tendency terms of accretion of species y by species x in terms of mass mixing ratio and number concentration, respectively. V_t is the terminal velocity. $\left(\frac{\rho_0}{\rho_a}\right)^{\frac{1}{2}}$ is the air density correction term, as used in Lin et al. (1983), to allow for increasing fall speeds with increasing altitude (decreasing air density). ρ_0 is the reference air density and ρ_a is the air density. Some studies (e.g., Reisner et al., 1998) do not consider the air density correction term while other studies use different correction formulae, e.g., $\left(\frac{\rho_0}{\rho_a}\right)^{0.54}$ from Heymsfield et al. (2007) is used in

SZ11. E_{xy} is the collection efficiency. N_T is the total number concentration. λ is the spectral slope parameter, μ is the shape parameter, and N_0 is the intercept parameter of the gamma distribution. $\mathrm{M}(D_y) = a_{my} D_y^{b_{my}} \rho_y$ represents the mass of a single particle y. ρ_y is the density of particle y. The value of terminal velocity difference in the double integral makes integration very difficult (Wisner et al., 1972). Therefore, Mizuno (1990), Murakami (1990) and Wisner et al. (1972) simplified the integration of the general collection equations. Assumed to be independent of diameter, the mass- and number-weighted terminal velocity for each of species x and y are computed and taken outside the double integral. For example, $\Delta\overline{V_m} = |V_{mx} - V_{my}|$ and $\Delta\overline{V_n} = |V_{nx} - V_{ny}|$ follows Wisner et al. (1972). A similar idea was applied in Mizuno (1990) and Murakami (1990) except for a more complex form. Processes of collision between rain and snow and collection of snow by rain in Ikawa and Saito (1990), Reisner et al. (1998), Gettelman et al. (2019) and SZ11 use the representation of $\Delta\overline{V_m}$ from Mizuno (1990).

Starting from the general continuous collection equations, we derive production terms for rimed ice below.

The increase (decrease) in q_s (q_c) due to accretion of cloud droplets by snow is given as

$$P_{sacw}^{qc} = \frac{\pi a_{vs} \rho_a q_c E_{cs} N_{0s} \Gamma(b_{vs}+3)}{4\lambda_s^{b_{vs}+3}} \tag{b3}$$

and the decrease in N_c is given as

$$P_{sacw}^{Nc} = \frac{\pi a_{vs} \rho_a N_c E_{cs} N_{0s} \Gamma(b_{vs}+3)}{4\lambda_s^{b_{vs}+3}} \tag{b4}$$

This is derived by assuming that $D_s \gg D_c$, $V_{ts} \gg V_{tc}$, and $V_{ts} = a_{vs} D^{b_{vs}}$, which is used in Thompson et al. (2004), MG08, and SZ11, and many others. E_{cs} is the collection efficiency for droplet-snow collision and is calculated based on the Stokes number dependent on the mean radii of the cloud droplets and snow, following MG08. The amount of rime on snow converted to rimed ice is written below following the derivation from Ikawa and Saito (1990)

$$P_{g.sacw}^{qs} = \Delta\mathrm{t}\frac{3\rho_0 \pi N_{0s}(\rho_a q_c)^2 E_{cs}^2 a_{vs}^2 \Gamma(2b_{vs}+2)}{\rho_a(\rho_g-\rho_s)\lambda_s^{2b_{vs}+2}} \quad \text{(b5)}$$

$$P_{g.sacw}^{Ns} = 8\Delta t\frac{\rho_0}{\rho_a}\left[\frac{3\pi a_{vs}\rho_a q_c E_{cs}}{2(\rho_g-\rho_s)}\right]^2 \frac{N_{0s}}{\lambda_s} \quad \text{(b6)}$$

$\Delta\mathrm{t}$ is time step. equation (b5) is derived by integrating the dispatcher function and riming growth of snow over the entire size distribution spectrum. The purpose of the dispatch function is to specify the portion of the accreted cloud water to be converted to graupel (see Ikawa and Saito, 1990 for more details). The increase of graupel number concentration by riming of snow is given in equation (b6) integrating the probability for a snow particle of diameter *D* to be converted into a graupel particle and the number concentration of snow particle over the entire size distribution spectrum (see Ikawa and Saito, 1990 for more details).

The amount of snow converted to rimed ice as embryo is written below following Ikawa and Saito (1990)

$$P_{scng}^{qs} = \frac{\rho_s}{\rho_g-\rho_s}P_{g.sacw}^{qs} \quad \text{(b7)}$$

Production of rimed ice through collection of cloud droplets by rimed ice is given as

$$P_{g.gacw}^{qc} = \frac{\pi a_{vg}\rho_a q_c E_{cg} N_{0g}\Gamma(b_{vg}+\mu_g+3)}{4\lambda_g^{b_{vg}+\mu_g+3}} \quad \text{(b8)}$$

$$P_{g.gacw}^{Nc} = \frac{\pi a_{vg}\rho_a N_c E_{cg} N_{0g}\Gamma(b_{vg}+\mu_g+3)}{4\lambda_g^{b_{vg}+\mu_g+3}} \quad \text{(b9)}$$

This is derived by assuming that $D_g \gg D_c$, $V_{tg} \gg V_{tc}$, and $V_{tg} = a_{vg}D^{b_{vg}}$. E_{cg} is the collection efficiency for droplet-graupel collision and is assumed to be unity. Equation (b8) differs from that in Lin et al. (1983) (their Eq. 40) and Reisner et al. (1998) (their Eq. A.59) only in the consideration of the shape parameter of rimed ice. We also derive the change of number concentration of cloud droplets due to collection [Eq. (b9)] based on the geometric sweeping out concept.

Production of rimed ice through collection of rain water by rimed ice is given as:

$$P_{g.gacr}^{qr} = \frac{\pi^2}{4} E_{gr} N_{0g} N_{0r} \Delta\overline{V_m} \left(\frac{\rho_0}{\rho_a}\right)^{\frac{1}{2}} \frac{\rho_w}{\rho_a} \left[\frac{\Gamma(3+\mu_g)}{\lambda_g^{3+\mu_g} \lambda_r^4} + \frac{8\Gamma(2+\mu_g)}{\lambda_g^{2+\mu_g} \lambda_r^5} + \frac{20\Gamma(1+\mu_g)}{\lambda_g^{1+\mu_g} \lambda_r^6}\right] \quad \text{(b10)}$$

$$P_{g.gacr}^{Nr} = \frac{\pi}{4} E_{gr} N_{0g} N_{0r} \Delta\overline{V_n} \left(\frac{\rho_0}{\rho_a}\right)^{\frac{1}{2}} \left[\frac{\Gamma(3+\mu_g)}{\lambda_g^{3+\mu_g} \lambda_r} + \frac{2\Gamma(2+\mu_g)}{\lambda_g^{2+\mu_g} \lambda_r^2} + \frac{2\Gamma(1+\mu_g)}{\lambda_g^{1+\mu_g} \lambda_r^3}\right] \quad \text{(b11)}$$

This is derived by assuming that raindrops are spherical. E_{gr} is the collection efficiency for raindrop-graupel collision and assumed to be unity. We set $\Delta\overline{V_m} = |V_{mg} - V_{mr}|$ and $\Delta\overline{V_n} = |V_{ng} - V_{nr}|$ following Wisner et al. (1972).

Collection of rain by snow as well as collection of snow by rain are as follows

$$P_{sacr}^{qr} = \pi^2 E_{sr} N_{0s} N_{0r} \Delta\overline{V_m} \frac{\rho_w}{\rho_a} \left[\frac{0.5}{\lambda_s^3 \lambda_r^4} + \frac{2}{\lambda_s^2 \lambda_r^5} + \frac{5}{\lambda_s\ \lambda_r^6}\right] \quad \text{(b12)}$$

$$P_{sacr}^{Nr} = \frac{\pi}{2} E_{sr} N_{0s} N_{0r} \Delta\overline{V_n} \left[\frac{1}{\lambda_s^3 \lambda_r} + \frac{1}{\lambda_s^2 \lambda_r^2} + \frac{1}{\lambda_s\ \lambda_r^3}\right] \quad \text{(b13)}$$

$$P_{racs}^{qs} = \frac{\pi}{4} a_{ms} E_{sr} N_{0s} N_{0r} \Delta\overline{V_m} \frac{\rho_s}{\rho_a} \left[\frac{2\Gamma(1+b_{ms})}{\lambda_r^3 \lambda_s^{1+b_{ms}}} + \frac{2\Gamma(2+b_{ms})}{\lambda_r^2 \lambda_s^{2+b_{ms}}} + \frac{\Gamma(3+b_{ms})}{\lambda_r\ \lambda_s^{3+b_{ms}}}\right] \quad \text{(b14)}$$

P_{sacr}^{qr} and P_{sacr}^{Nr} are derived by assuming spherical raindrops. E_{sr} is the collection efficiency for raindrop-snow collision and is assumed to be unity. In calculating P_{racs}^{qs}, the parameters (a_{ms}, b_{ms}) in the snow mass-diameter relationship are kept in the general form. $\Delta\overline{V_m} = [(1.2V_{mr} - 0.95V_{ms})^2 + 0.08V_{mr}V_{ms}]^{0.5}$, $\Delta\overline{V_n} = [1.7(V_{mr} - V_{ms})^2 + 0.3V_{mr}V_{ms}]^{0.5}$ following Mizuno (1990), as in Gettelman et al. (2019) and Reisner et al. (1998).

Production of rimed ice through collection of rain by snow as well as collection of snow by rain following Ikawa and Saito (1990) and Reisner et al. (1998) is as follows

$$P^{qs}_{g.sacr} = (1-\alpha)P^{qr}_{sacr} \quad \text{(b15)}$$

$$P^{Ns}_{g.sacr} = (1-\alpha)P^{Nr}_{sacr} \quad \text{(b16)}$$

$$P^{qs}_{g.racs} = (1-\alpha)P^{qs}_{racs} \quad \text{(b17)}$$

$$\alpha = \frac{\rho_s^2(\frac{4}{\lambda_s})^6}{\rho_s^2(\frac{4}{\lambda_s})^6+\rho_w^2(\frac{4}{\lambda_r})^6} \quad \text{(b18)}$$

Appendix C – *Microphysics budget equations from SZ11*

Equations c1-c8 below are the mass mixing ratio and number concentration budget equations 3-10 in Song and Zhang (2011). Here we use different symbols from SZ11 to be consistent with the budget equations in this work. Note that there are a few typos in the budget equations 4, 8 and 10 in Song and Zhang (2011). For instance, there should be a number change of cloud liquid droplets due to the Bergeron process (P^{Nc}_{Berg}) but this term is not included in their equation 4, and there should not be a number change of rain due to accretion with cloud water (P^{Nc}_{accr}) and of snow due to accretion with cloud ice, cloud water and rain (P^{Ni}_{accs}, P^{Nc}_{accs}, P^{Nr}_{accs}) but these terms are written in their equations 8 and 10. We have corrected the budget equations (see our c4 and c8 equations) here.

$$S^q_c = P^{qc}_{c.cond} - P^{qc}_{c.auto} - P^{qc}_{racw} - P^{qc}_{c.frz\_hom} - P^{qc}_{c.frz\_het} - P^{qc}_{Berg} - P^{qc}_{sacw} \quad \text{(c1)}$$

$$S^N_c = P^{Nc}_{c.act} - P^{Nc}_{c.auto} - P^{Nc}_{racw} - P^{Nc}_{c.frz\_hom} - P^{Nc}_{c.frz_{het}} - P^{Nc}_{sacw} - P^{Nc}_{Berg} \quad \text{(c2)}$$

$$S^q_r = P^{qc}_{c.auto} + P^{qc}_{racw} - P^{qr}_{r.fallout} - P^{qr}_{sacr} - P^{qr}_{r.frz\_hom} - P^{qr}_{r.frz\_het} \quad \text{(c3)}$$

$$S^N_r = P^{Nc}_{c.auto} - P^{Nr}_{r.fallout} - P^{Nr}_{r.agg} - P^{Nr}_{sacr} - P^{Nr}_{r.frz\_hom} - P^{Nr}_{r.frz\_het} \quad \text{(c4)}$$

$$S^q_i = P^{qi}_{i.dep} + P^{qc}_{c.frz\_hom} + P^{qc}_{c.frz\_het} + P^{qc}_{Berg} - P^{qi}_{i.auto} - P^{qi}_{saci} \quad \text{(c5)}$$

$$S^N_i = P^{Ni}_{i.nul} + P^{Nc}_{c.frz\_hom} + P^{Nc}_{c.frz\_het} - P^{Ni}_{i.auto} - P^{Ni}_{saci} \quad \text{(c6)}$$

$$S^q_s = P^{qi}_{i.auto} + P^{qi}_{saci} + P^{qc}_{sacw} + P^{qr}_{sacr} - P^{qs}_{s.fallout} + P^{qr}_{r.frz\_hom} + P^{qr}_{r.frz\_het} \quad \text{(c7)}$$

$$S_s^N = P_{i.auto}^{Ni} - P_{s.agg}^{Ns} - P_{s.fallout}^{Ns} + P_{r.frz\_hom}^{Nr} + P_{r.frz\_het}^{Nr} \quad \text{(c8)}$$

Note that the Song and Zhang (2011) water budget equations (Eq c1-c8) omit explicit terms for snow melting and rain evaporation. Convective cloud microphysics is dealing with microphysical processes in the saturated updrafts. Cloud microphysics in unsaturated downdrafts has not been included. Instead, Rain evaporation is handled based on the Sundqvist (1988) scheme in the ZM95 convection scheme outside the SZ11 convective cloud microphysics when precipitation particles fall out of the saturated updrafts. Regarding snow melting, it is also not treated in the SZ11 cloud microphysics scheme because all microphysical processes in a convective framework are integrated from bottom to top following updraft flows. Snow, whose vertical profile is provided by SZ11 convective microphysics, is transported top-down in the ZM95 convection scheme into a warm environment to melt.

Appendix D – *List of symbols*

In the following, SZ11 refers to Song and Zhang (2011), R98 to Reisner et al., (1998), L83 to Lin et al., (1983), IS90 to Ikawa and Saito (1990), EL17 to Elsaesser et al., (2017). Note that even though we direct readers to specific publications below, it does not necessarily mean that the expressions are directly developed or derived from that publications. Readers are recommended to refer to specific publications for more details on the origin of the parameters and expressions.

Notation	Description
a_s	Parameter in $V_t = a_s D^{b_s}$ for snow; used in microphysical processes except sedimentation. $a_s = 11.72 m^{1-b_s} s^{-1}$
b_s	Parameter in $V_t = a_s D^{b_s}$ for snow; used in microphysical processes except sedimentation. $b_s = 0.41$

a_g	Parameter in $V_t = a_g D^{b_g}$ for rimed ice; used in microphysical processes except sedimentation. $a_g = 19.3\ m^{1-b_g} s^{-1}$
b_g	Parameter in $V_t = a_g D^{b_g}$ for rimed ice; used in microphysical processes except sedimentation. b_g =0.37
α_i	Parameter in the XReICE sedimentation parameterization for cloud ice; used only in sedimentation. See Table 1.
β_i	Parameter in the XReICE sedimentation parameterization for cloud ice; used only in sedimentation. See Table 1.
α_s	Parameter in the EL17 sedimentation parameterization for snow; used only in sedimentation. See Table 1.
β_s	Parameter in the EL17 sedimentation parameterization for snow; used only in sedimentation. See Table 1.
α_g	Parameter in the EL17 sedimentation parameterization for rimed ice; used only in sedimentation. See Table 1.
β_g	Parameter in the EL17 sedimentation parameterization for rimed ice; used only in sedimentation. See Table 1.
ρ_i	Bulk density of cloud ice = 500 kg m^{-3}
ρ_s	Bulk density of snow = 100 kg m^{-3}
ρ_g	Bulk density of rimed ice = 500 kg m^{-3}
μ_g	Shape parameter of rimed ice (= 3) in the gamma distribution
q_c	Mass mixing ratio of cloud water
q_i	Mass mixing ratio of cloud ice

q_r	Mass mixing ratio of rain
q_s	Mass mixing ratio of snow
q_g	Mass mixing ratio of rimed ice
N_c	Number concentration of cloud water
N_i	Number concentration of cloud ice
N_r	Number concentration of rain
N_s	Number concentration of snow
N_g	Number concentration of rimed ice
$P_{c.act}^{Nc}$	Generation rate of N_c by activation on aerosol (SZ11)
$P_{c.auto}^{Nc}$	Depletion rate of N_c by cloud water autoconversion to rain (SZ11)
$P_{c.auto}^{qc}$	Generation (depletion) rate of q_r (q_c) by cloud water autoconversion to rain (SZ11)
P_{Berg}^{qc}	Generation (depletion) rate of q_i (q_c) by Bergeron-Findeisen process (SZ11)
$P_{c.cond}^{qc}$	Generation rate of q_c by condensation (SZ11)
$P_{c.frz\_het}^{qc}$	Depletion (generation) rate of q_c (q_i) by cloud water heterogeneous freezing (SZ11)
$P_{c.frz\_het}^{Nc}$	Depletion (generation) rate of N_c (N_i) by cloud water heterogeneous freezing (SZ11)
$P_{c.frz\_hom}^{qc}$	Depletion (generation) rate of q_c (q_i) by cloud water homogeneous freezing (SZ11)
$P_{c.frz\_hom}^{Nc}$	Depletion (generation) rate of N_c (N_i) by cloud water homogeneous freezing (SZ11)
$P_{g.gacw}^{Nc}$	Depletion rate of N_c by accretion of cloud water by rimed ice (this study, see Eq. b9)
$P_{g.gacw}^{qc}$	Generation rate of q_g by accretion of cloud water (this study, see Eq. b8)
P_{racw}^{Nc}	Depletion rate of N_c by accretion of cloud water with rain (SZ11)
P_{racw}^{qc}	Generation (depletion) rate of q_r (q_c) by accretion (SZ11)
P_{sacw}^{Nc}	Depletion rate of N_c by accretion of cloud water with snow (SZ11)

P_{sacw}^{qc}	Generation (depletion) rate of q_s (q_c) by accretion (SZ11)
$P_{r.agg}^{Nr}$	Depletion rate of N_r due to self-collection of raindrops (SZ11)
$P_{r.fallout}^{qr}$	Depletion rate of q_r due to fallout (SZ11)
$P_{r.fallout}^{Nr}$	Depletion rate of N_r due to fallout (SZ11)
$P_{r.frz\_het}^{qr}$	Depletion (generation) rate of q_r (q_g) by rain heterogeneous freezing (SZ11-modified to be source of q_g in this study)
$P_{r.frz\_het}^{Nr}$	Depletion (generation) rate of N_r (N_g) by rain heterogeneous freezing (SZ11-modified to be source of N_g in this study)
$P_{r.frz\_hom}^{qr}$	Depletion (generation) rate of q_r (q_g) by rain homogeneous freezing (SZ11-modified to be source of q_g in this study)
$P_{r.frz\_hom}^{Nr}$	Depletion (generation) rate of N_r (N_g) by rain homogeneous freezing (SZ11-modified to be source of N_g in this study)
$P_{g.gacr}^{Nr}$	Depletion rate of N_r by accretion of rain by rimed ice (this study, see Eq. b11)
$P_{g.gacr}^{qr}$	Generation rate of q_g by accretion of rain (this study, see Eq. b10)
$P_{g.racs}^{qs}$	Generation rate of q_g by that portion of collected snow by rain which is converted into rimed ice (R98)
P_{sacr}^{Nr}	Depletion rate of N_r by accretion of rain with snow (SZ11)
P_{sacr}^{qr}	Generation (depletion) rate of q_s (q_r) by accretion (SZ11)
$P_{i.auto}^{Ni}$	Generation (depletion) rate of q_s (q_i) by cloud ice autoconversion to snow (SZ11)
$P_{i.auto}^{qi}$	Generation (depletion) rate of q_s (q_i) by cloud ice autoconversion to snow (SZ11)
P_{scng}^{qs}	Generation (depletion) rate of q_g (q_s) due to the collection of cloud water by snow (R98, originally IS90)

$P_{i.nul}^{Ni}$	Generation rate of N_i by ice nucleation (SZ11)
$P_{i.dep}^{qi}$	Generation rate of q_i by deposition (SZ11)
$P_{i.fallout}^{qi}$	Depletion rate of q_i due to fallout (this study, XReICE)
$P_{i.fallout}^{Ni}$	Depletion rate of N_i due to fallout (this study, XReICE)
P_{saci}^{qi}	Generation (depletion) rate of q_s (q_i) by accretion of cloud ice (SZ11)
P_{saci}^{Ni}	Depletion rate of N_i by accretion of cloud ice by snow (SZ11)
$P_{s.agg}^{Ns}$	Depletion rate of N_s due to self-collection of snow particles (SZ11)
$P_{s.fallout}^{Ns}$	Depletion rate of N_s due to fallout (EL17)
$P_{s.fallout}^{qs}$	Depletion rate of q_s due to fallout (EL17)
$P_{g.sacr}^{Ns}$	Generation rate of N_g by collision between rain and snow (R98, see Eq. b16)
$P_{g.sacr}^{qs}$	Generation rate of q_g by that portion of collected rain by snow which is converted into rimed ice (R98, see Eq. b15)
$P_{g.sacw}^{Ns}$	Generation rate of N_g by collision between cloud water and snow (R98, see Eq. b6)
$P_{g.sacw}^{qs}$	Generation rate of q_g by that portion of collected cloud water by snow which is converted into rimed ice (R98, see Eq. b5)
$P_{g.fallout}^{Ng}$	Depletion rate of N_g due to fallout (EL17)
$P_{g.fallout}^{qg}$	Depletion rate of q_g due to fallout (EL17)

Appendix E

Table E1. EL17 coefficients for convective snow and rimed ice.

V_m coefficients

Convective snow[1]				Rimed ice[2]			
V_{m1}	V_{m2}	V_{m3}	V_{m4}	V_{m1}	V_{m2}	V_{m3}	V_{m4}
-3.137	0.022	0.084	-0.246	-3.329	0.025	0.189	-0.244

[1]see Table 1 of Elsaesser et al. (2017). [2]see text in section 2.2.1 for details.

Acknowledgements. This study is supported by the U.S. Department of Energy (DOE) Atmospheric System Research (ASR) Program (Office of Science, OBER) under Grant #DE-SC0018190 and the Climate Model Development and Validation (CMDV) program. This paper has been authored by employees of Brookhaven Science Associates, LLC, under contract #DE-SC0012704 with the U.S. DOE. The contributions by GSE are supported by DOE/ASR Grant #DE-SC0020192. The publisher by accepting the paper for publication acknowledges that the United States Government retains a nonexclusive, paid-up, irrevocable, worldwide license to publish or reproduce the published form of this paper, or allow others to do so, for United States Government purposes. We wish to thank Alain Protat (Bureau of Meteorology) and Christopher Williams (University of Colorado Boulder) for providing Darwin profiler vertical velocity retrievals to generate CFAD examples, as adapted from those found in Kumar et al. (2015). Authors would like to acknowledge the use of computational resources (doi:10.5065/D6RX99HX) at the NCAR-Wyoming Supercomputing Center provided by the National Science Foundation and the State of Wyoming and supported by NCAR's Computational and Information Systems Laboratory. The DOE-ARM TWP-ICE observational dataset used for this study is available from the DOE ARM discovery website (https://www.archive.arm.gov/discovery/). EOS MLS data can be download from website https://mls.jpl.nasa.gov/. Three-dimensional IWC data can be download from https:/doi.org/10.5281/zenodo.3758515. The CAM5 simulation outputs for this study are available online (https:/doi.org/10.5281/zenodo.3758515). We would like to thank Dr. Mattew Gilmore and another anonymous reviewer for their constructive comments to help improve the manuscript.

References

Arakawa, A. and W. H. Schubert (1974), Interaction of A Cumulus Cloud Ensemble with the Large-scale Environment. Part I, Journal of the Atmospheric Sciences, 31, 674–701.

Baker, B., and R. P. Lawson (2006), Improvement in Determination of Ice Water Content from Two-dimensional Particle Imagery. Part I: Image-to-mass Relationship, *Journal of Applied Meteorology and Climatology*, 45, 1282-1290, doi:10.1175/JAM2398.1.

Betts, A. K. (1986), A New Convective Adjustment Scheme. Part I: Observational and theoretical basis, *Quarterly Journal of the Royal Meteorological Society*, 112, 677–691.

Biggerstaff, M. I., and R. A. Houze Jr (1991), Kinematic and Precipitation Structure of the 10-11 June 1985 Squall Line, *Monthly Weather Review*, 119, 3034-3065.

Bony, S., R. Colman, V. M. Kattsov, R. P. Allan, C. S. Bretherton, J.-L. Dufresne, et al. (2006), How Well Do We Understand and Evaluate Climate Change Feedback Processes? *Journal of Climate*, 19(15), 3445–3482. https://doi.org/10.1175/JCLI3819.1.

Dai, A. (2006), Precipitation Characteristics in Eighteen Coupled Climate Models, *Journal of Climate*, 19, 4605-4630.

Danabasoglu, G., Lamarque, J.-F., Bacmeister, J., Bailey, D. A., DuVivier, A. K., Edwards, J., et al. (2020), The Community Earth System Model Version 2 (CESM2), *Journal of*

Advances in Modeling Earth Systems, 12, e2019MS001916. https://doi.org/ 10.1029/2019MS001916

Deng, M., G. G., Mace and Z. Wang (2016), Anvil Productivities of Tropical Deep Convective Clusters and Their Regional Differences, *Journal of the Atmospheric Sciences*, 72, 3467–3487. DOI: 10.1175/JAS-D-15-0239.1

Elsaesser, G. S., A. D. Del Genio, J. H. Jiang, and M. van Lier-Walqui (2017), An Improved Convective Ice Parameterization for the NASA GISS Global Climate Model and Impacts on Cloud Ice Simulation, *Journal of Climate*, 30(1), 317-336, doi:10.1175/jcli-d-16-0346.1.

Emanuel, K. A. (1991), A Scheme for Representing Cumulus Convection in Large-scale Models, *Journal of the Atmospheric Sciences*, 48, 2313–2335.

Falk, N. M., A. L. Igel, and M. R. Igel (2019), The Relative Impact of Ice Fall Speeds and Microphysics Parameterization Complexity on Supercell Evolution, *Monthly Weather Review*, 147(7), 2403-2415, doi:10.1175/mwr-d-18-0417.1.

Fu, Q., S. Krueger, K. N. Liou (1995), Interactions of Radiation and Convection in Simulated Tropical Cloud Clusters, *Journal of the Atmospheric Sciences*, 52(9), 1310-1328.

Gamache, J. F., and R. A. Houze (1983), Water Budget of a Mesoscale Convective System in the Tropics. *Journal of the Atmospheric Sciences*, 40, 1835–1850, doi:10.1175/1520-0469(1983)040, 1835:WBOAMC.2.0.CO;2.

Gettelman, A., H. Morrison, K. Thayer-Calder, and C. M. Zarzycki (2019), The Impact of Rimed Ice Hydrometeors on Global and Regional Climate, *Journal of Advances in Modeling Earth Systems*, 11(6), 1543-1562, doi:10.1029/2018ms001488.

Ghan, S., and Coauthors (2000), A Comparison of Single Column Model Simulations of Summertime Midlatitude Continental Convection. *Journal of Geophysical Research*, 105(D2), 2091–2124.

Giangrande, S. E., T. Toto, M. P. Jensen, M. J. Bartholomew, Z. Feng, A. Protat, C. R. Williams, C. Schumacher, and L. Machado (2016), Convective Cloud Vertical Velocity and Mass-flux Characteristics from Radar Wind Profiler Observations during GoAmazon2014/5, *Journal of Geophysical Research: Atmospheres*, 121(21), 12,891-812,913, doi:10.1002/2016jd025303.

Golaz, J.-C., Caldwell, P. M., Van Roekel, L. P., Petersen, M. R., Tang, Q., Wolfe, J. D., et al. (2019), The DOE E3SM coupled model version 1: Overview and evaluation at standard resolution. *Journal of Advances in Modeling Earth Systems*, 11, 2089–2129. https://doi.org/10.1029/2018MS001603

Gunn, R., and G.D. Kinzer (1949), The Terminal Velocity of Fall for Water Droplets in Stagnant Air, *Journal of Meteorology*, 6, 243–248.

Hartmann, D. L. (2016), Tropical Anvil Clouds and Climate Sensitivity, *Proceedings of the National Academy of Sciences of the United States of America*, 113(32), 8897-8899, doi:10.1073/pnas.1610455113.

Hartmann, D. L., and K. Larson (2002), An Important Constraint on Tropical Cloud - Climate Feedback, *Geophysical Research Letters*, 29(20), 12-11-12-14, doi:10.1029/2002gl015835.

Heymsfield, A. (1972), Ice Crystal Terminal Velocities, *Journal of the Atmospheric Sciences*, 29, 1348–1357, https://doi.org/10.1175/1520-0469(1972)029<1348:ICTV>2.0.CO;2

Heymsfield, A. J., C. Schmitt, and A. Bansemer (2013), Ice Cloud Particle Size Distributions and Pressure-Dependent Terminal Velocities from In Situ Observations at Temperatures from 0° to −86°C, *Journal of the Atmospheric Sciences*, 70(12), 4123-4154, doi:10.1175/jas-d-12-0124.1.

Heymsfield, A. J., and C. D. Westbrook (2010), Advances in the Estimation of Ice Particle Fall Speeds Using Laboratory and Field Measurements, *Journal of the Atmospheric Sciences*, 67(8), 2469-2482, doi:10.1175/2010jas3379.1.

Heymsfield, A. and R. Wright (2014), Graupel and Hail Terminal Velocities: Does a “Supercritical” Reynolds Number Apply?. *Journal of the Atmospheric Sciences*, 71, 3392–3403, https://doi.org/10.1175/JAS-D-14-0034.1

Houze, R. A., Jr., (1997), Stratiform Precipitation in Regions of Convection: A Meteorological Paradox?, *Bulletin of the American Meteorological Society*, 78, 2179–2196, https://doi.org/10.1175/1520-0477(1997)078<2179:SPIROC>2.0.CO;2.

Hurrell, J., and Coauthors (2013), The Community Earth System Model: A framework for Collaborative Research. *Bulletin of the American Meteorological Society*, 94, 1339–1360, doi:10.1175/BAMS-D-12-00121.1.

Ikawa, M., & Saito, K. (1990). Description of the nonhydrostatic model developed at the Forecast Research Department of the MRI. Tech. Rep. 28, Meteorological Institute MRI.

Jackson, R. C., G. M. McFarquhar, A. M. Fridlind, and R. Atlas (2015), The Dependence of Cirrus Gamma Size Distributions Expressed as Volumes in N0-λ-μ Phase Space and Bulk Cloud Properties on Environmental Conditions: Results from the Small Ice Particles in Cirrus Experiment (SPARTICUS), *Journal of Geophysical Research: Atmospheres*, 120(19), doi:10.1002/2015jd023492.

Jiang, J. H., and Coauthors (2012), Evaluation of Cloud and Water Vapor Simulations in CMIP5 Climate Models Using NASA "A-Train" Satellite Observations, *Journal of Geophysical Research: Atmospheres*, 117, D14105, doi:10.1029/2011jd017237.

Khvorostyanov, V. I., and J. A. Curry (2002), Terminal Velocities of Droplets and Crystals: Power Laws with Continuous Parameters over the Size Sectrum, *Journal of the Atmospheric Sciences*, 59, 1872-1884.

Krueger, S.K., Q. Fu, K.N. Liou, and H.N.S. Chin (1995), Improvement of an ice-phase microphysics parameterization for use in numerical simulations of tropical convection. *Journal of Applied Meteorology*, 34, 281-287.

Kumar, V. V., C. Jakob, A. Protat, C. R. Williams, and P. T. May (2015), Mass-Flux Characteristics of Tropical Cumulus Clouds from Wind Profiler Observations at Darwin, Australia, *Journal of the Atmospheric Sciences*, 72(5), 1837-1855, doi:10.1175/jas-d-14-0259.1.

Kuo, H.-L. (1965), On the Formation and Intensification of Tropical Cyclones through Latent Heat Release by Cumulus Convection. *Journal of the Atmospheric Sciences*, 22, 40–63.

Lamb, D., and J. Verlinde (2011), Physics and Chemistry of Clouds, Cambridge Univ. Press, Cambridge, U. K.

Li J.-L. F., D.E. Waliser, W.-T. Chen, B. Guan, T. Kubar, et al. (2012), An observationally based evaluation of cloud ice water in CMIP3 and CMIP5 GCMs and contemporary reanalyses using contemporary satellite data, *Journal of Geophysical Research*, 117, D16105, doi:10.1029/2012JD017640.

Li, X.W., W.-K. Tao, A. Khain, J. Simpson, and D. Johnson (2009), Sensitivity of a cloud-resolving model to the bulk and explicit bin microphysical schemes. Part I. Comparisons. *Journal of the Atmospheric Sciences*, 66, 3-21.

Lin, Y., L. J. Donner, and B. A. Colle (2011), Parameterization of Riming Intensity and Its Impact on Ice Fall Speed Using ARM Data, *Monthly Weather Review*, 139(3), 1036-1047, doi:10.1175/2010mwr3299.1.

Lin, Y.-L., R. D. Farley, and H. D. Orville (1983), Bulk Parameterization of the Snow Field in a Cloud Model. *Journal of Climate and Applied Meteorology*, 22, 1065–1092.

Lindzen, R. S., M.-D. Chou, and A. Y. Hou (2001), Does the Earth Have An Adaptive Infrared Iris?, *Bulletin of the American Meteorological Society*, 82(417-432), 417-.

Liu, X., J. Penner, S. Ghan, and M. Wang (2007), Inclusion of Ice Microphysics in the NCAR Community Atmospheric Model Version 3(CAM3), *Journal of Climate*, 20, 4526-4547.

Liu, X., S. Xie, J. Boyle, S. A. Klein, Shi, X., Wang, Z., Lin, W.,Ghan, S. J., Earle, M., Liu, P. S. K., and Zelenyuk, A. (2011), Testingcloud microphysics parameterizations in NCAR CAM5 with IS-DAC and M-PACE observations, *Journal of Geophysical Research - Atmosphere*, 116,D00T11,doi:10.1029/2011JD015889.

Livesey, N. J., W. G. Read, P. A. Wagner, L. Froidevaux, A. Lambert and et al. (2018), Earth Observing System (EOS) Aura Microwave Limb Sounder (MLS), Version 4.2x Level 2 data quality and description document, Tech. Rep. JPL D-33509, Tech. Rep. version 4.2x-3.1, NASA Jet Propulsion Laboratory, 2018.

Locatelli, J. D., and P. V. Hobbs (1974), Fall Speeds and Masses of Solid Precipitation Particles, *Journal of Geophysical Research*, 79(15), 2185-2197, doi:10.1029/JC079i015p02185.

Lohmann, U., and E. Roeckner (1996), Design and Performance of A New Cloud Microphysical Scheme Developed for the ECHAM General Circulation Model, *Climate Dynamics*, 12, 557-572.

Luo, Y., S. Krueger, and K. Xu (2005), Cloud Properties Simulated by A Single-column Model. Part II: Evaluation of Cumulus Detrainment and Ice-Phase Microphysics Using a Cloud-Resolving Model, *Journal of the Atmospheric Sciences*, 63, 2831-2847.

May, P. T., J. H. Mather, G. Vaughan, C. Jakob, G. M. McFarquhar, K. N. Bower, and G. G. Mace (2008), The Tropical Warm Pool International Cloud Experiment, *Bulletin of the American* Meteorological Society, 89(5), 629-646, doi:10.1175/bams-89-5-629.

Mather, J. H. and Voyles, J. W. (2013), The Arm Climate Research Facility: A Review of Structure and Capabilities, *Bulletin of the American Meteorological Society*, 94, 377–392.

Minnis, P., W. L. Smith Jr, D. F. Young, L. Nguyen, A. D. Rapp, P. W. Heck, and M. M. Khaiyer (2002), Near-real-time Retrieval of Cloud Properties over the ARM CART Area from GOES Data, paper presented at the 12th ARM Science Team Meeting, ARM, St Petersburg, Fla., 8-12 April.

Mitchell, D. L. (1996), Use of Mass- and Area-Dimensional Power Laws for Determining Precipitation Particle Terminal Velocities, *Journal of the Atmospheric Sciences*, 53(12), 1710-1723.

Mizuno, H. (1990), Parameterization of the accretion process between different precipitation elements. *Journal of the Meteorological Society of Japan*, 68, 395-398.

Morrison, H., and A. Gettelman (2008), A New Two-Moment Bulk Stratiform Cloud Microphysics Scheme in the Community Atmosphere Model, Version 3 (CAM3). Part I:

Description and Numerical Tests, *Journal of Climate*, 21(15), 3642-3659, doi:10.1175/2008jcli2105.1.

Murakami, M. (1990), Numerical modeling of dynamical and microphysical evolution of an isolated convective cloud – the 19 July 1981 CCOPE cloud. *Journal of the Meteorological Society of Japan*, 68, 107-128.

Pruppacher, H. R., and J. D. Klett (1996), Microphysics of Clouds and Precipitation, D. Reidel, Norwell, Mass.

Qian, Y., H. Yan, Z. Hou, G. Johannesson, S. Klein, et al. (2015), Parametric Sensitivity Analysis of Precipitation at Global and Local Scales in the Community Atmosphere Model CAM5, *Journal of Advances in Modeling Earth Systems.*, 7(2), 382-411, doi:10.1002/2014ms000354.

Ramanathan, V., and W. Collins (1991), Thermodynamic Regulation of Ocean Warming by Cirrus Clouds Deduced from Obsrevations of the 1987 El Nino, *Nature*, 351, 27-32.

Randall, D. A., K. M. Xu, R. J. C. Somerville, and S. Iacobellis (1996), Single-column Models and Cloud Ensemble Models as Links between Observations and Climate Models. *Journal of Climate*, 9(8), 1683– 1697.

Reisner, J., R. M. Rasmussen, and R. T. Bruintjes (1998), Explicit Forecasting of Supercooled Liquid Water in Winter Storms Using the MM5 Mesoscale Model, *Quarterly Journal of the Royal Meteorological Society*, 124, 1071-1107.

Rutledge, S. A., and R. A. Houze Jr (1987), A Diagnostic Modeling Study of the Trailing Stratiform Region of a Midlatitude Squall Line, *Journal of the Atmospheric Sciences*, 44(18), 2640-2656.

Seo, E.-K., and G. Liu (2005), Retrievals of Cloud Ice Water Path by Combining Ground Cloud Radar and Satellite High-frequency Microwave Measurements near the ARM SGP Site, *Journal of Geophysical Research: Atmospheres*, 110(D14), doi:10.1029/2004jd005727.

Seo E.-K, and G. Liu (2006), Determination of 3D Cloud Ice Water Contnets by Combining Multiple Data Sources from Satellite, Ground Radar, and a Numerical Model, *Journal of Applied Meteorology and Climatology*, 45, 1494-1504.

Shan, Y. P., E. Wilcox, L. Gao, L. Lin, D. Mitchell, et al. (2020), Evaluating Errors in Gamma-Function Representations of the Raindrop Size Distribution: A Method for Determining the Optimal Parameter Set for Use in Bulk Microphysics Schemes, *Journal of the Atmospheric Sciences*, 77, 513-529, DOI: 10.1175/JAS-D-18-0259.1

Slingo, J. M., and Coauthors, (1994), Mean climate and transience in the Tropics of the UGAP GCM: Sensitivity to convective parameterization. *Quart. J. Roy. Meteor. Soc*, **120 ,** 881–922.

Smull, B. F., and R. A. Houze Jr (1985), A Midlatitude Squall Line with a Trailing Region of Stratiform Rain: Radar and Satellite Observation, *Monthly Weather Review*, 113, 117-133.

Song, X., and G. J. Zhang (2011), Microphysics Parameterization for Convective Clouds in A Global Climate Model: Description and Single-column Model Tests, *Journal of Geophysical Research*, 116(D2), doi:10.1029/2010jd014833.

Song, X., G. J. Zhang, and J. L. F. Li (2012), Evaluation of Microphysics Parameterization for Convective Clouds in the NCAR Community Atmosphere Model CAM5, *Journal of Geophysical Research*, 25(24), 8568-8590, doi:10.1175/jcli-d-11-00563.1.

Steiner, M., R. A. Houze Jr., and S. E. Yuter (1995), Climatological Characterization of Three-Dimensional Storm Structure from Operational Radar and Rain Gauge Data. *Journal of Applied Meteor*ology, 34, 1978–2007, https://doi.org/10.1175/1520-0450(1995)034<1978:CCOTDS>2.0.CO;2.

Stephens, G. L. (2005), Cloud Feedbacks in the Climate System: A Critical Review, *Journal of Climate*, *18*, 237-273.

Stith, J. L., J. E. Dye, A. Bansemer, A. J. Heymsfield, C. A. Grainger, W. A. Petersen, and R. Cifelli (2002), Microphysical Observations of Tropical Clouds. *Journal of Applied Meteor*ology, 41, 97–117.

Storer, R. L., G. J. Zhang, and X. Song (2015), Effects of Convective Microphysics Parameterization on Large-Scale Cloud Hydrological Cycle and Radiative Budget in Tropical and Midlatitude Convective Regions, *Journal of Climate*, *28*(23), 9277-9297, doi:10.1175/jcli-d-15-0064.1.

Straka, J. (2009), Cloud and Precipitation Microphysics: Principles and Parameterizations. Cambridge University Press, 9-10 pp.

Takahashi, H., Zhengzhao. J. Luo, and G. L. Stephens (2017), Level of Neutral Buoyancy, Deep Convective Outflow, and Convective Core: New Perspectives based on 5 Years of CloudSat Data. *Journal of Geophysical Research: Atmospheres*, 122, 2958-2969, doi:10.1002/2016JD025969.

Tao, W.-K., J.-P. Chen, Z. Li, C. Wang, and C. Zhang (2012), Impact of Aerosols on Convective Clouds and Precipitation, *Reviews of Geophysics*, 50, RG200. https://doi.org/10.1029/2011RG000369

Tiedtke, M. (1989), A Comprehensive Mass Flux Scheme for Cumulus Parameterization in Large-scale Models, *Monthly Weather Review*, 117, 1779–1800.

Varble, A., and Coauthors (2011), Evaluation of Cloud-Resolving Model Intercomparison Simulations Using TWP-ICE Observations: Precipitation and Cloud Structure. *Journal of Geophysical Research*, 116, D12206. https://doi.org/10.1029/2010JD015180.

Waliser, D. E., and Coauthors (2009), Cloud Ice: A Climate Model Challenge with Signs and Expectations of Progress, *Journal of Geophysical Research*, 114, D00A21, doi:10.1029/2008JD010015.

Wang, D., S. E. Giangrande, K. Schiro, M. P. Jensen, and R. A. Houze (2019), The Characteristics of Tropical and Midlatitude Mesoscale Convective Systems as Revealed by Radar Wind Profilers. *Journal of Geophysical Research: Atmospheres*,124, 4601–4619. https://doi.org/10.1029/2018JD030087

Wang, D., Jensen, M. P., D'Iorio, J. A., Jozef, G., Giangrande, S. E., Johnson, K.L., et al. (2020). An observational comparison of level of neutral buoyancy and level of maximum detrainment in tropical deep convective clouds. *Journal of Geophysical Research: Atmospheres*,125, e2020JD032637. https://doi.org/10.1029/2020JD032637

Wang, W., X. Liu, S. Xie, J. Boyle, and S. A. McFarlane (2009), Testing Ice Microphysics Parameterizations in the NCAR Community Atmospheric Model Version 3 Using Tropical Warm Pool–International Cloud Experiment Data, *Journal of Geophysical Research*, *114*(D14), doi:10.1029/2008jd011220.

Williams, C. R. (2012), Vertical Air Motion Retrieved from Dual-Frequency Profiler Observations. *Journal of Atmospheric and Oceanic Technology*, 29(10), 1471– 1480. https://doi.org/10.1175/JTECH-D-11-00176.1

Wisner, C. E., H. D. Orville and C. G. Myers (1972), A numerical model of a hail bearing cloud, *Journal of Atmospheric Science*, 29, 1160-1181.

Wu, D., X. Dong, B. Xi, Z. Feng, A. Kennedy, G. Mullendore, M. Gilmore, and W.-K. Tao (2013), Impacts of Microphysical Scheme on Convective and Stratiform Characteristics in Two High Precipitation Squall Line Events, *Journal of Geophysical Research: Atmospheres*, *118*(19), 11,119-111,135, doi:10.1002/jgrd.50798.

Xie, S., T. Hume, C. Jakob, S. A. Klein, R. B. McCoy, and M. Zhang (2010), Observed Large-Scale Structure and Diabatic Heating and Drying Profiles during TWP-ICE. *Journal of Climate*, 23, 57–79, https://doi.org/10.1175/2009JCLI3071.1.

Yuter, S. E., and R. A. Houze (1995), Three-dimensional Kinematic and Microphysical Evolution of Florida Cumulonimbus. Part II: Frequency Distributions of Vertical Velocity, Reflectivity, and Differential Reflectivity, *Monthly Weather Review*, 123, 1941–1963.

Zeng, X., W.-K. Tao, S. W. Powell, R. A. Houze, P. Ciesielski, N. Guy, H. Pierce and T. Matsui (2013), A Comparison of the Water Budget between Clouds from AMMA and TWP-ICE, *Journal of the Atmospheric Sciences*, 70, 487-503, doi:10.1175/JAS-D-12-050.1.

Zhang, G. J., and N. A. McFarlane (1995), Sensitivity of Climate Simulations to the Parameterization of Cumulus Convection in the Canadian Climate Centre General Circulation Model, *Atmosphere-Ocean*, 33(3), 407–446. https://doi.org/10.1080/07055900.1995.9649539.

Zhang, J., U. Lohmann, and P. Stier (2005), A Microphysical Parameterization for Convective Clouds in the ECHAM5 Climate Model: Single-column Model Results Evaluated at the

Oklahoma Atmospheric Radiation Measurement Program Site, *Journal of Geophysical Research*, 110(D15), doi:10.1029/2004jd005128.

Zhang, M., J. Lin, R. T. Cederwall, J. J. Yio, and S. C. Xie (2001), Objective Analysis of ARM IOP Data: Method and Sensitivity. *Monthly Weather Review*, 129(2), 295– 311. https://doi.org/10.1175/1520-0493(2001)129<0295:OAOAID>2.0.CO;2.

Zhang, M. H., and J. L. Lin (1997), Constrained Variational Analysis of Sounding Data Based on Column-Integrated Budgets of Mass, Heat, Moisture, and Momentum: Approach and Application to Arm Measurements. *Journal of the Atmospheric Sciences*, 54(11), 1503–1524. https://doi.org/10.1175/1520-0469(1997)054.

Table 1. Prefactor (α) and exponential factor (β) for the terminal velocity-diameter power-law relationships $Vt = \alpha D^{\beta}$.

	α	β
[1]Cloud ice (XReICE)	$0.0446\nu^{-1}\left(\frac{8ag}{\rho_a \pi}\right)$	$b-1$
Snow (EL17)	$\alpha_{Deq\_snow}(\frac{6a}{\pi\rho_w})^{\beta_{Deq\_snow}/3}$	$\frac{\beta_{Deq\_snow} b}{3}$
Rimed ice (EL17)	$\alpha_{Deq\_rimed}(\frac{6a}{\pi\rho_w})^{\beta_{Deq\_rimed}/3}$	$\frac{\beta_{Deq\_rimed} b}{3}$

[1]see Appendix A for detailed mathematical derivation to obtain α and β in the *X-Re* $\boldsymbol{V_t}$ parameterization.

ν is the kinematic viscosity of air. a and b are the coefficients of the $\mathrm{m} = aD^b$ relationships (see text for detail). ρ_a and ρ_w are the density of air and water, respectively. g is the gravitational acceleration. α_{Deq} and β_{Deq} are the coefficients in the terminal velocity-melted equivalent diameter power-law relationship, which are dependent on environmental conditions (see EL17 for detailed calculation). Since the EL17 scheme is developed in melted equivalent diameter space, conversion between melted equivalent diameter and maximum dimension is made for a comparison with other schemes developed in the maximum diameter space.

Table 2. Observed and simulated total, convective and stratiform mean rain rates (mm hr^{-1}) at the Darwin site during the active monsoon period (12 Z 19 – 12 Z 25 January 2006). The observational uncertainties with the lower and upper bounds are shown in the parentheses. The percentage contributions of convective and stratiform precipitation to the total are also given in the parentheses.

	Total	Convective	Stratiform
OBS[1]	1.077 (0.764-1.566)	0.668 (0.523-0.858) (62%)	0.409 (0.241-0.708) (38%)
CTRL	1.094	0.698 (64%)	0.396 (36%)
XReICE_EL17	1.116	0.709 (64%)	0.406 (36%)
XReICE_EL17_rime	1.109	0.712 (64%)	0.397 (36%)
Conv_snow_detr	1.109	0.696 (63%)	0.413 (37%)

[1] Observed total, convective and stratiform precipitation is estimated from Varble et al. (2011) by converting the volumetric rainfall rate to domain-mean values.

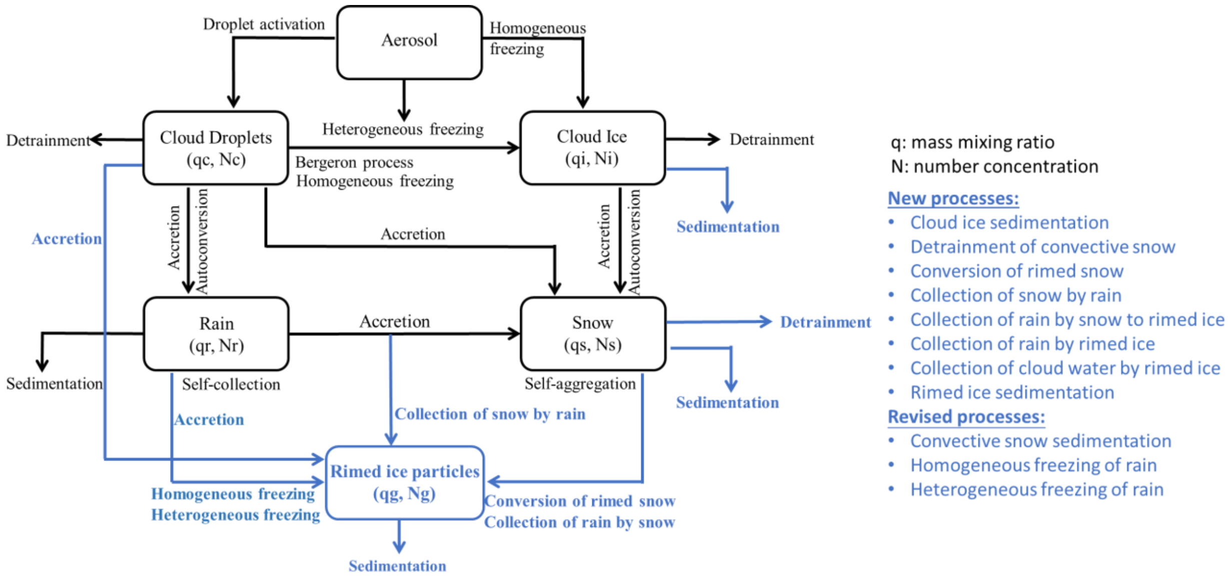

Figure 1. Schematic diagram of the microphysical processes considered in the convective clouds microphysics scheme. The processes originally treated in Song and Zhang (2011) are shown in black. New and modified processes are shown in blue. See text for more details.

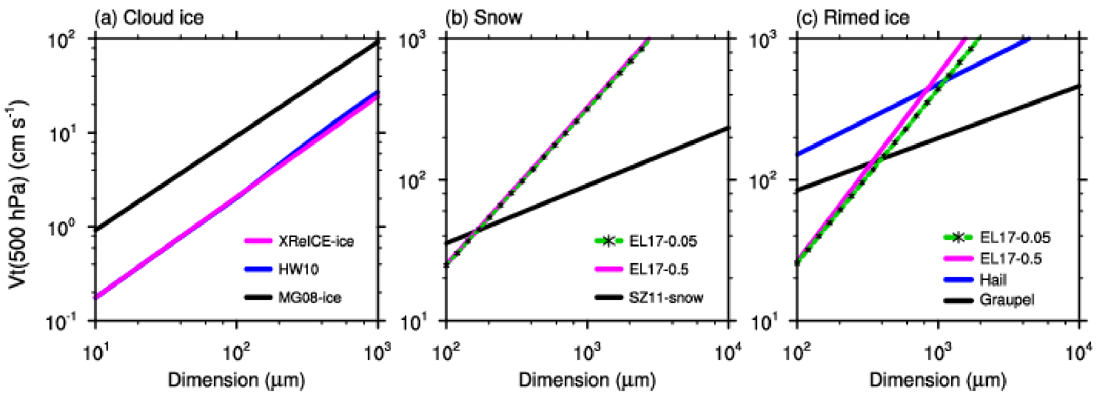

Figure 2. Cloud hydrometeor terminal velocity (V_t-D) (cm s^{-1}) for cloud ice crystals (a), snow particles (b) and rimed ice hydrometeors (c) as a function of particle maximum dimension (μm), at 500 hPa and -5 °C. The new schemes implemented in the model are the XReICE for cloud ice (XReICE-ice) and EL17 for snow and rimed ice (EL17-0.05/EL17-0.5) using a snow/rimed ice mixing ratio of 0.05 and 0.5 g kg^{-1}. The other schemes (e.g., MG08-ice: $V_t = 700D$; SZ11-snow: $V_t = 11.72D^{0.41}$; Hail: $V_t = 114.5D^{0.5}$; Graupel: $V_t = 19.3D^{0.37}$; all these equations, D are in meter) that are widely used in cloud models (e.g., stratiform cloud scheme, Morrison and Gettelman, 2008; Gettelman et al., 2019 and many others) are also shown for comparison. HW10 is the *X-Re* terminal velocity parameterization considering particle area ratio (Heymsfield and Westbrook, 2010); MG08-ice is the cloud ice terminal velocity parameterization used in Morrison and Gettelman (2008); Hail and graupel *Vt-D* relationships are from Matson and Huggins (1980) and Locatelli and Hobbs (1974), respectively.

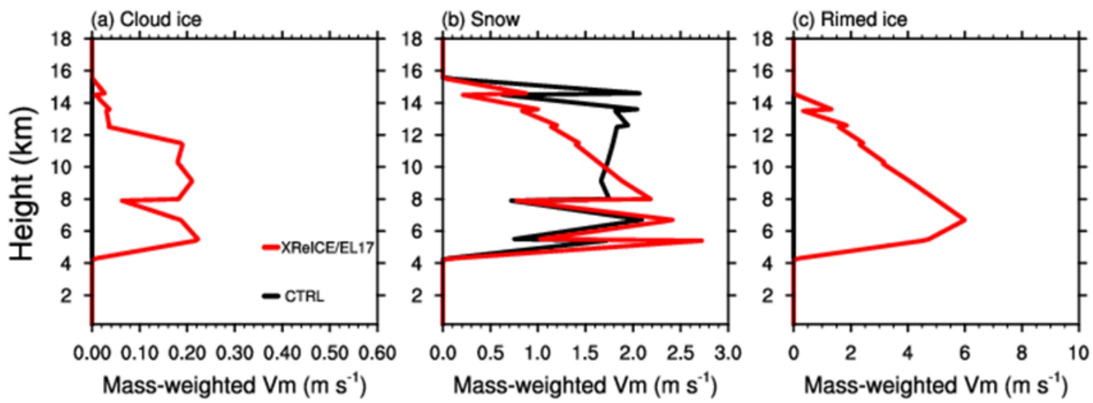

Figure 3. Vertical profiles of convective (a) cloud ice, (b) snow and (c) rimed ice mass-weighted terminal velocity averaged over the active monsoon period.

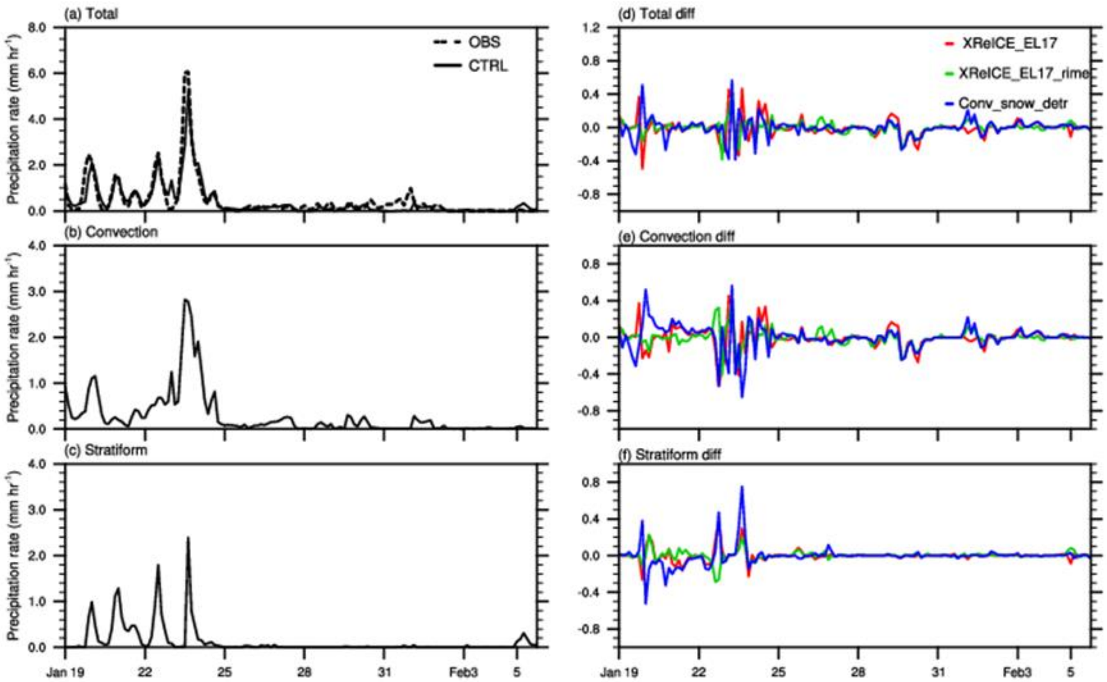

Figure 4. Time-series of (a) total, (b) convective and (c) stratiform precipitation rates (mm hr^{-1}) from observation and CTRL simulations during the TWP-ICE campaign, and (d)-(f) the corresponding differences between other experiments and CTRL.

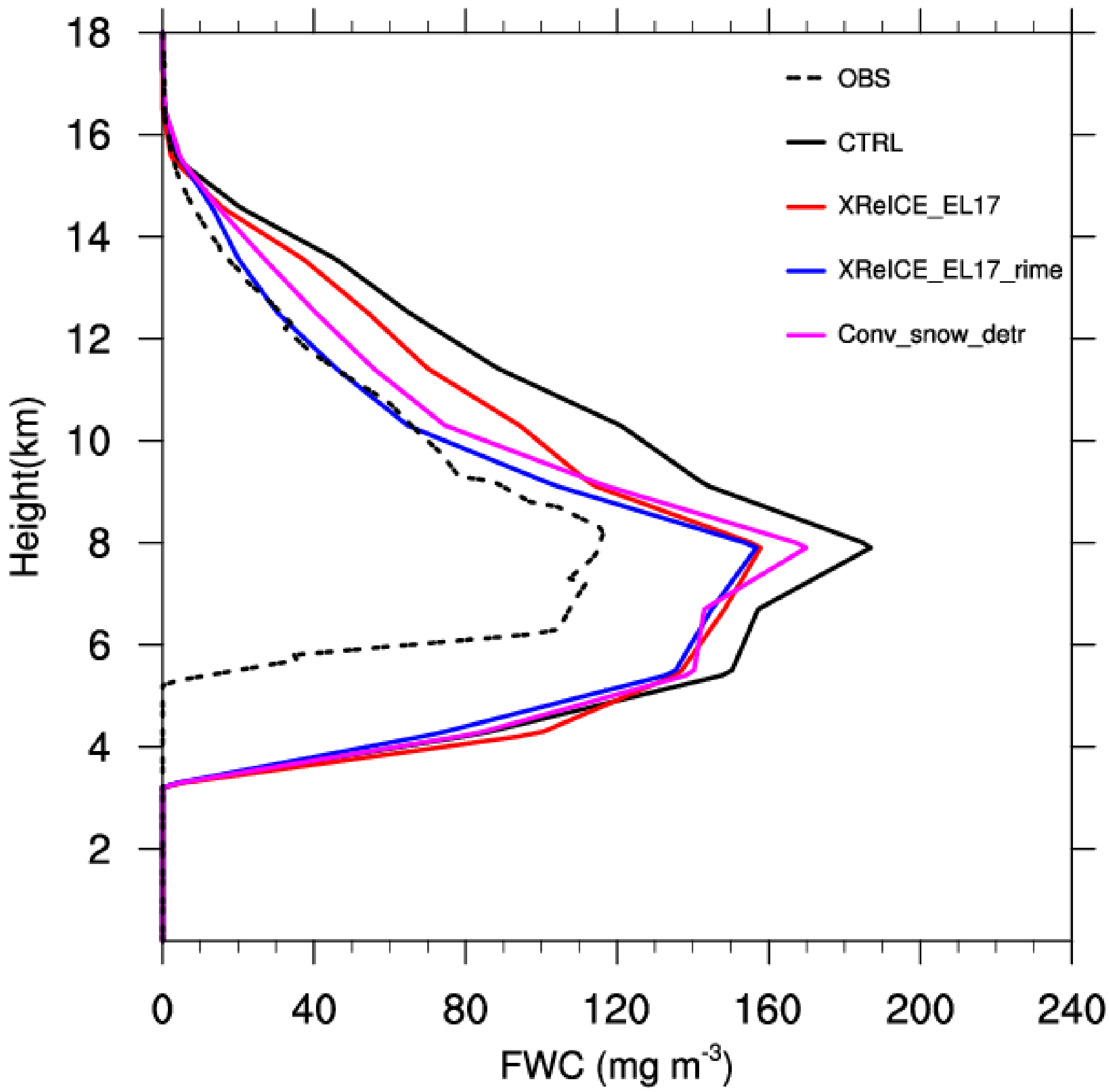

Figure 5. Vertical profiles of total frozen water content (FWC) (sum of convective and stratiform FWC) averaged over the active monsoon period.

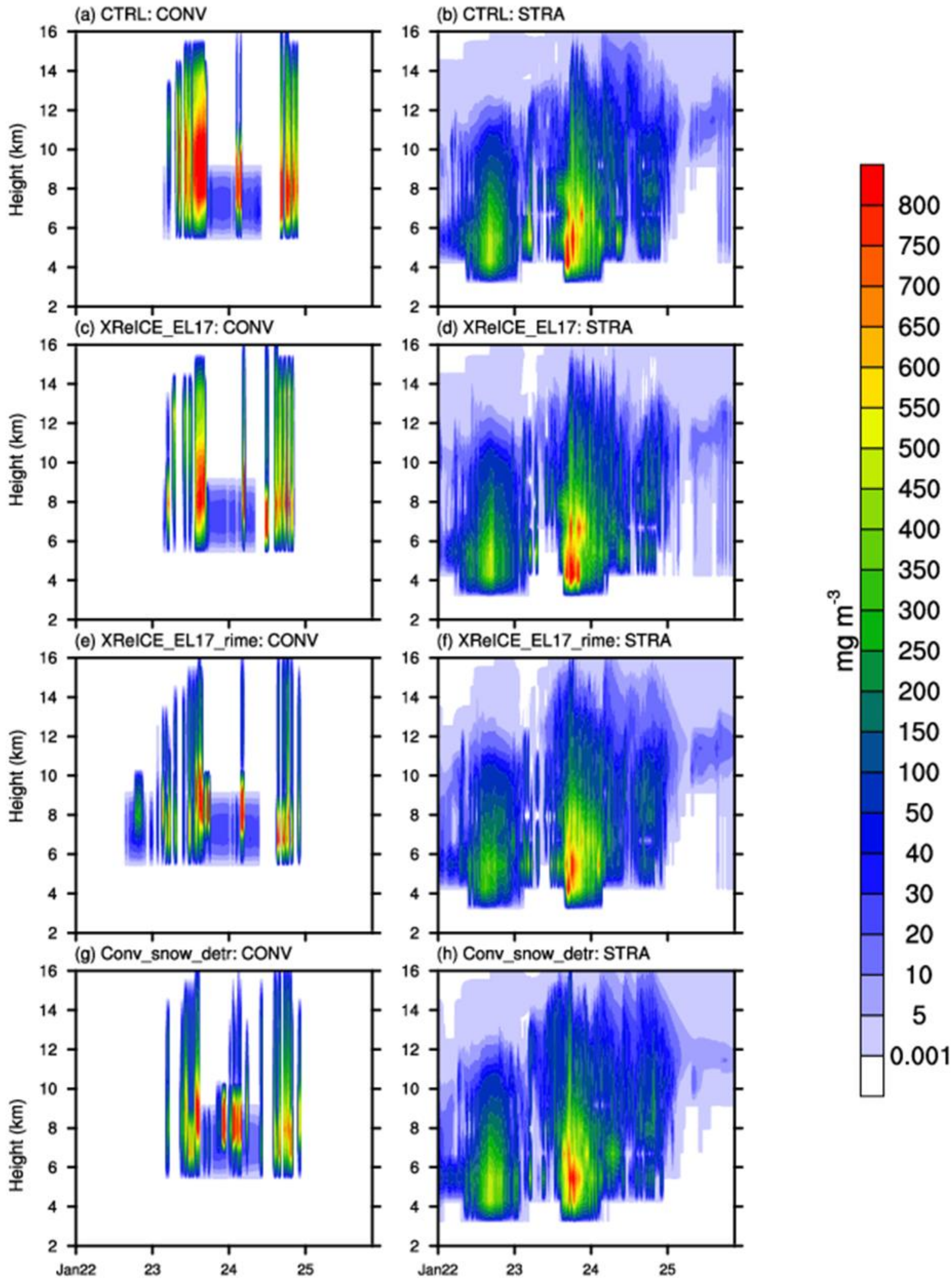

(a) CTRL: CONV
(b) CTRL: STRA
(c) XReICE_EL17: CONV
(d) XReICE_EL17: STRA
(e) XReICE_EL17_rime: CONV
(f) XReICE_EL17_rime: STRA
(g) Conv_snow_detr: CONV
(h) Conv_snow_detr: STRA
Height (km)
Jan22
23
24
25
mg m-3
800
750
700
650
600
550
500
450
400
350
300
250
200
150
100
50
40
30
20
10
5
0.001

Figure 6. Time-height cross-sections of convective (left) and stratiform (right) frozen water content (FWC) during the TWP-ICE active monsoon period from the CTRL (a-b), XReICE_EL17 (c-d), XReICE_EL17_rime (e-f) and Conv_snow_detr (g-h) simulations.

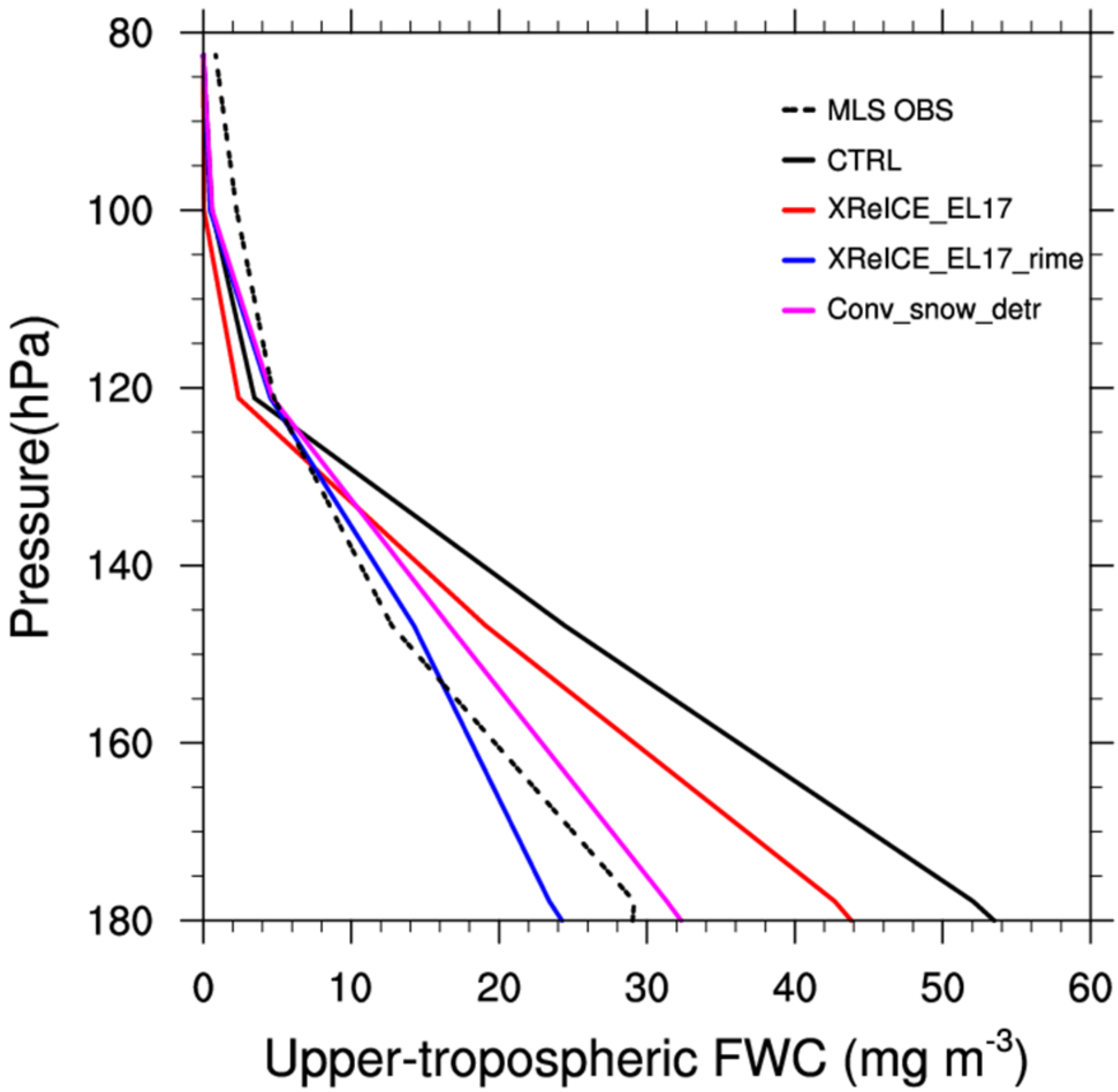

Figure 7. Vertical profiles of upper tropospheric total frozen water content (FWC) (sum of convective and stratiform FWC) averaged over the active monsoon period. Black dashed curve denotes Microwave Limb Sounder (MLS) observations.

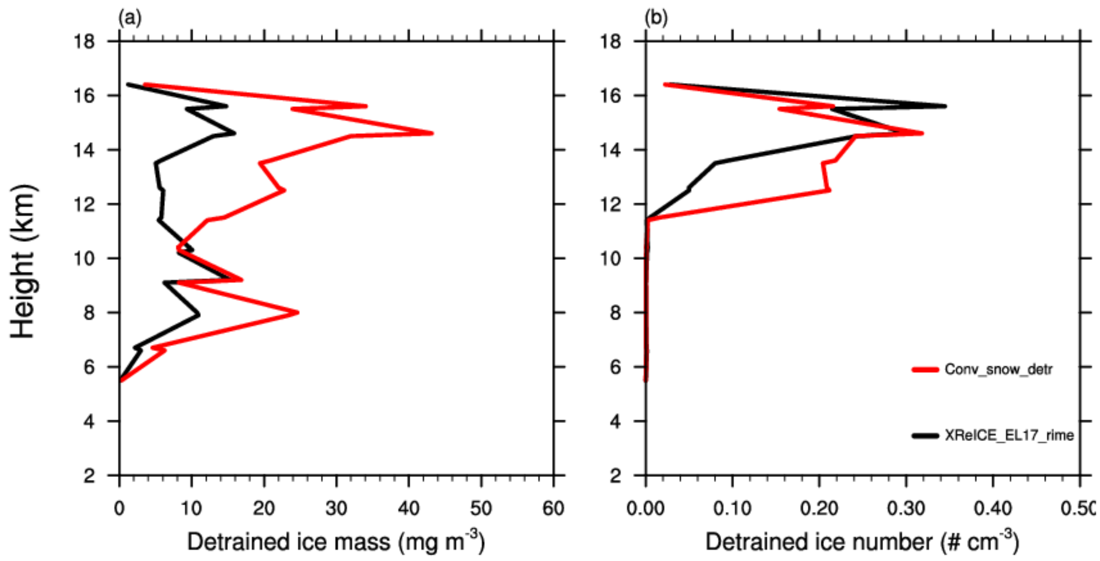

Figure 8. Vertical profiles of detrained ice mass mixing ratio (left) and number concentration (right) averaged over the active monsoon period (22-25 January 2006) from the XReICE_EL17_rime (black curve) and Conv_snow_detr (red curve) simulations.

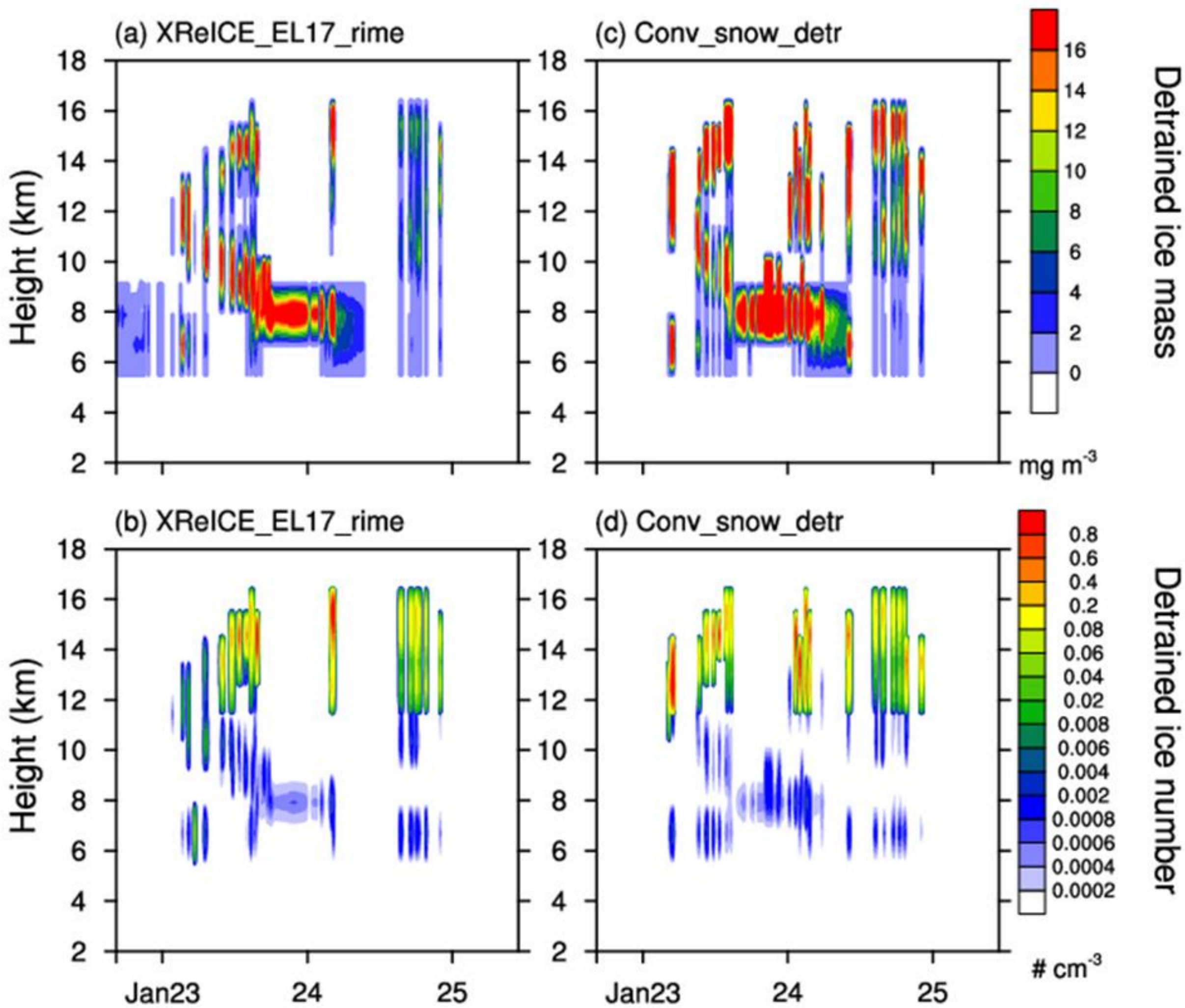

Figure 9. Time-height cross-section of detrained ice mass mixing ratio (top) and number concentration (bottom) from XReICE_EL17_rime (a-b) and Conv_snow_detr (c-d) simulations.

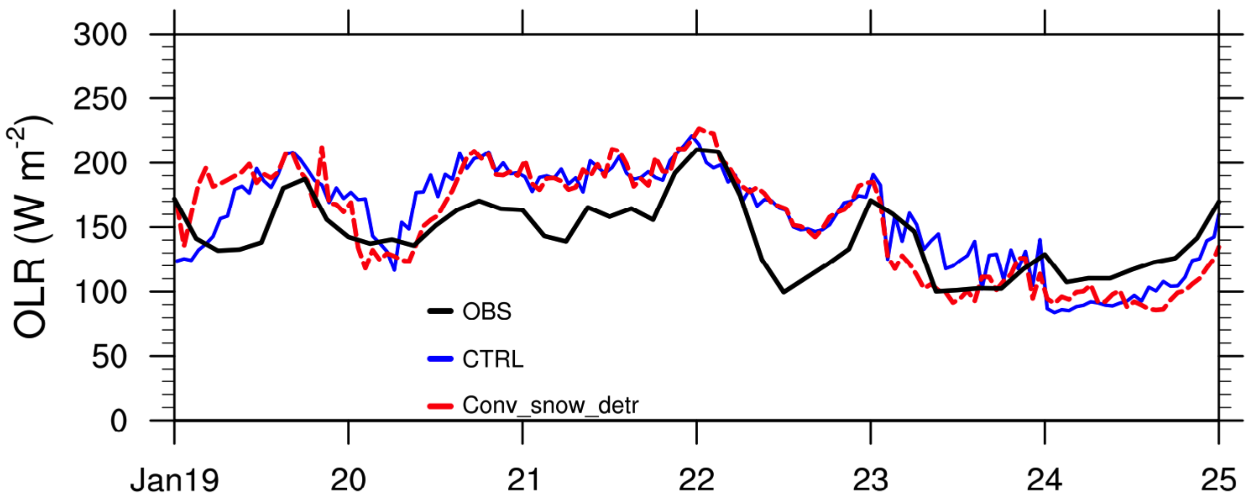

Figure 10. Top of the atmosphere (TOA) outgoing longwave radiation (OLR) for the CTRL (blue curve) and Conv_snow_detr (red curve) simulations, and from observations (black curve) during the active monsoon period.

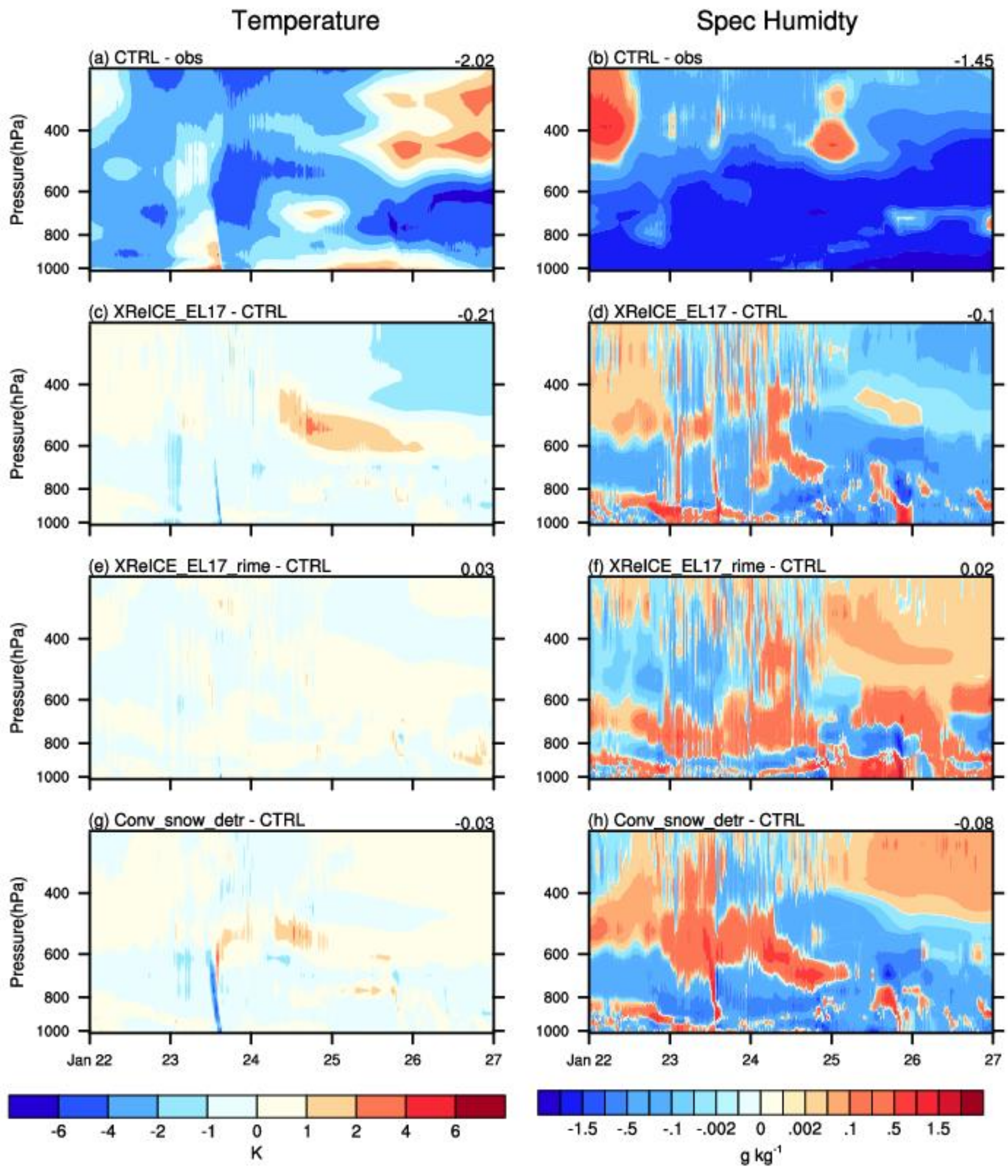

Figure 11. Time-pressure cross-section of temperature differences (left) and specific humidity differences (right) between (a, b) CTRL and observations, (c, d) XReICE_EL17 and CTRL, (e, f) XReICE_EL17_rime and CTRL, and (g, h) Conv_snow_detr and CTRL.

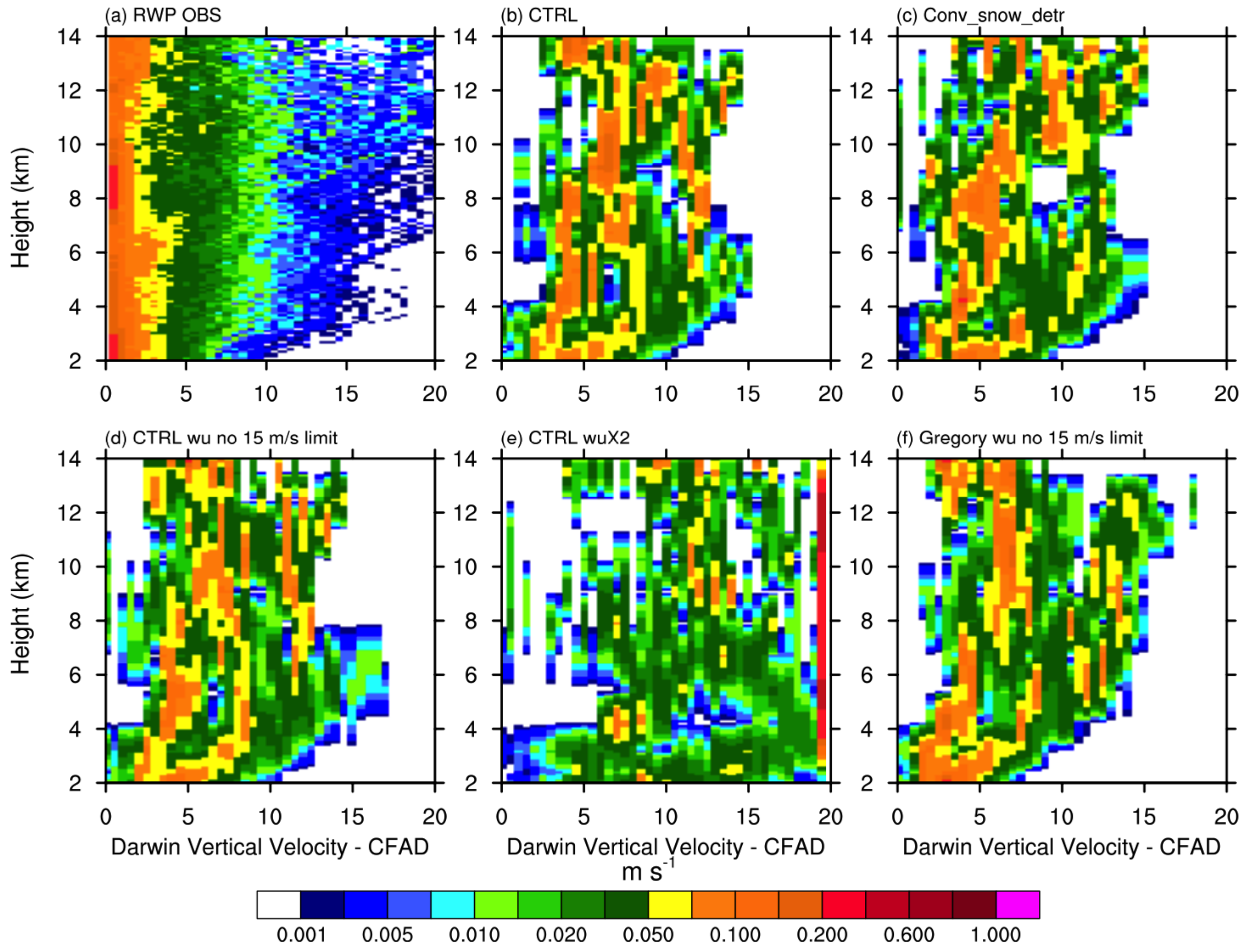

Figure 12. Normalized cumulative frequency by altitude diagram (CFAD) histograms of convective updraft vertical velocity at the Darwin site, Australia, from (a) radar wind profiler (RWP) data, (b) the control model (CTRL) simulation, (c) the Conv_snow_detr simulation, (d) the control simulation but with a removal of the 15 m s^{-1} upper bound in SZ11, (e) the control simulation but with a removal of the 15 m s^{-1} upper bound and with updrafts multiplied by two in SZ11, and (f) the convective updraft vertical velocity calculation replaced by Gregory (2001) with no 15 m s^{-1} upper bound. See text for additional details.

Figure1.

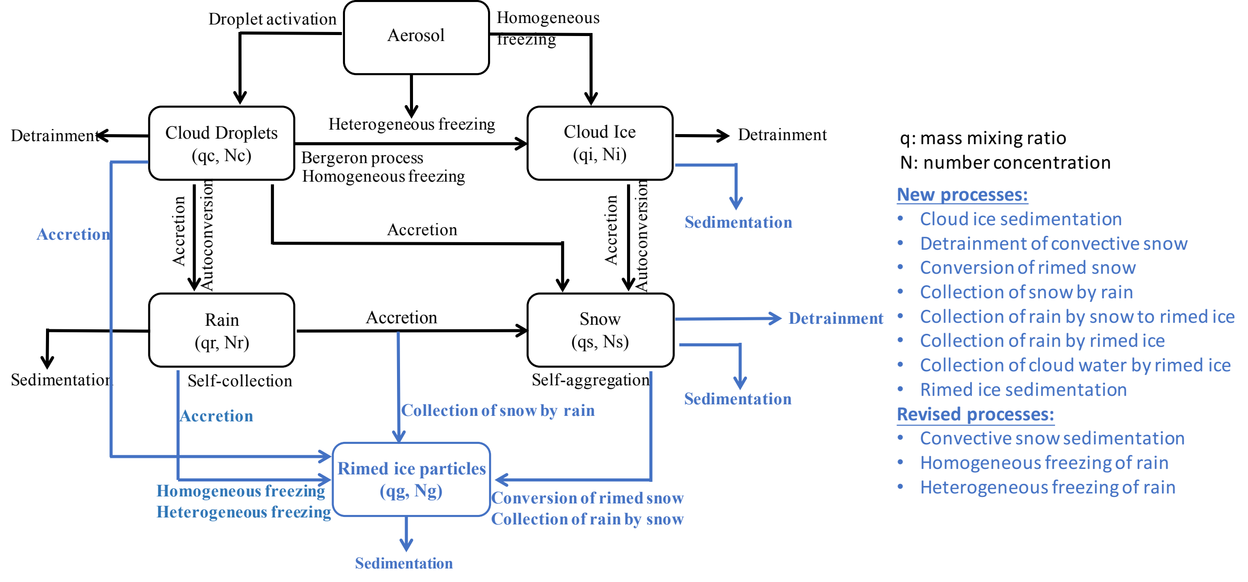

Aerosol
Droplet activation
Homogeneous freezing
Heterogeneous freezing
Cloud Droplets (qc, Nc)
Cloud Ice (qi, Ni)
Detrainment
Detrainment
Bergeron process
Homogeneous freezing
Accretion
Autoconversion
Accretion
Accretion
Autoconversion
Sedimentation
Accretion
Rain (qr, Nr)
Accretion
Snow (qs, Ns)
Detrainment
Sedimentation
Self-collection
Self-aggregation
Sedimentation
Accretion
Collection of snow by rain
Rimed ice particles (qg, Ng)
Homogeneous freezing
Heterogeneous freezing
Conversion of rimed snow
Collection of rain by snow
Sedimentation
q: mass mixing ratio
N: number concentration
New processes:
Cloud ice sedimentation
Detrainment of convective snow
Conversion of rimed snow
Collection of snow by rain
Collection of rain by snow to rimed ice
Collection of rain by rimed ice
Collection of cloud water by rimed ice
Rimed ice sedimentation
Revised processes:
Convective snow sedimentation
Homogeneous freezing of rain
Heterogeneous freezing of rain

Figure2.

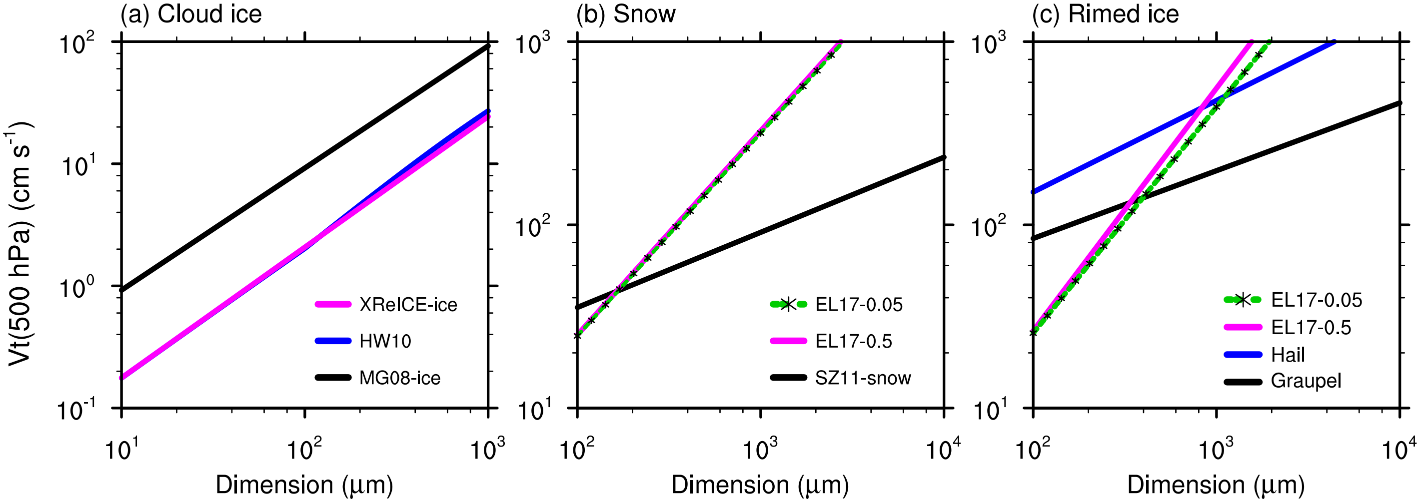

(a) Cloud ice
(b) Snow
(c) Rimed ice
Vt(500 hPa) (cm s-1)
Dimension (μm)
XReICE-ice
HW10
MG08-ice
EL17-0.05
EL17-0.5
SZ11-snow
Hail
Graupel

Figure3.

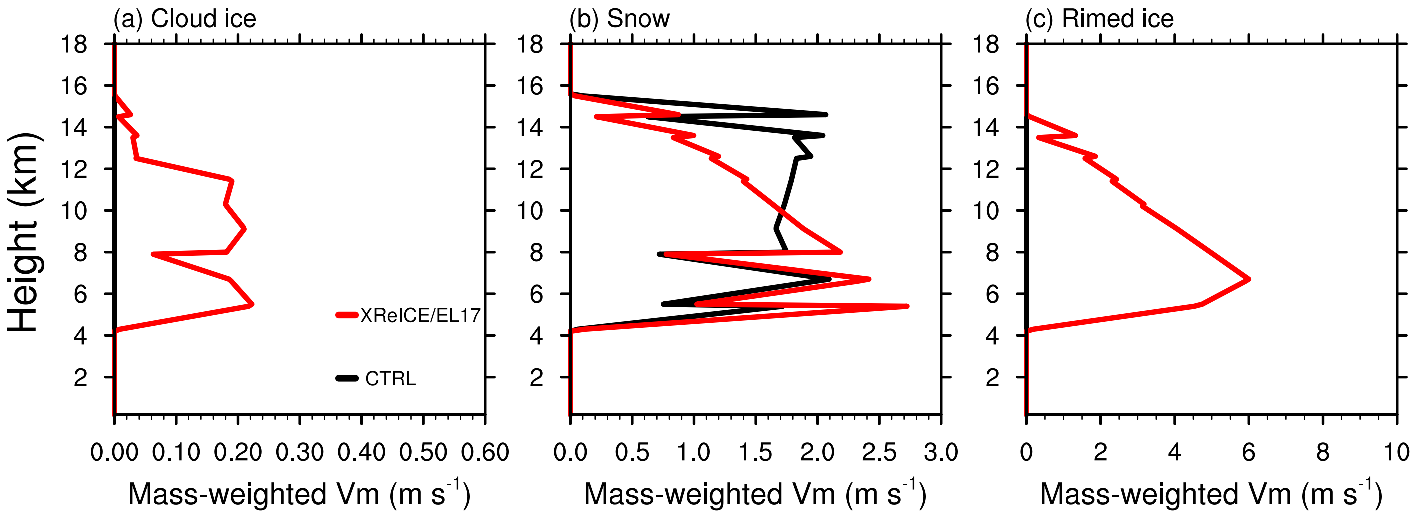

(a) Cloud ice
(b) Snow
(c) Rimed ice
Height (km)
18
16
14
12
10
8
6
4
2
XReICE/EL17
CTRL
0.00
0.10
0.20
0.30
0.40
0.50
0.60
0.0
0.5
1.0
1.5
2.0
2.5
3.0
0
2
4
6
8
10
Mass-weighted Vm (m s-1)

Figure4.

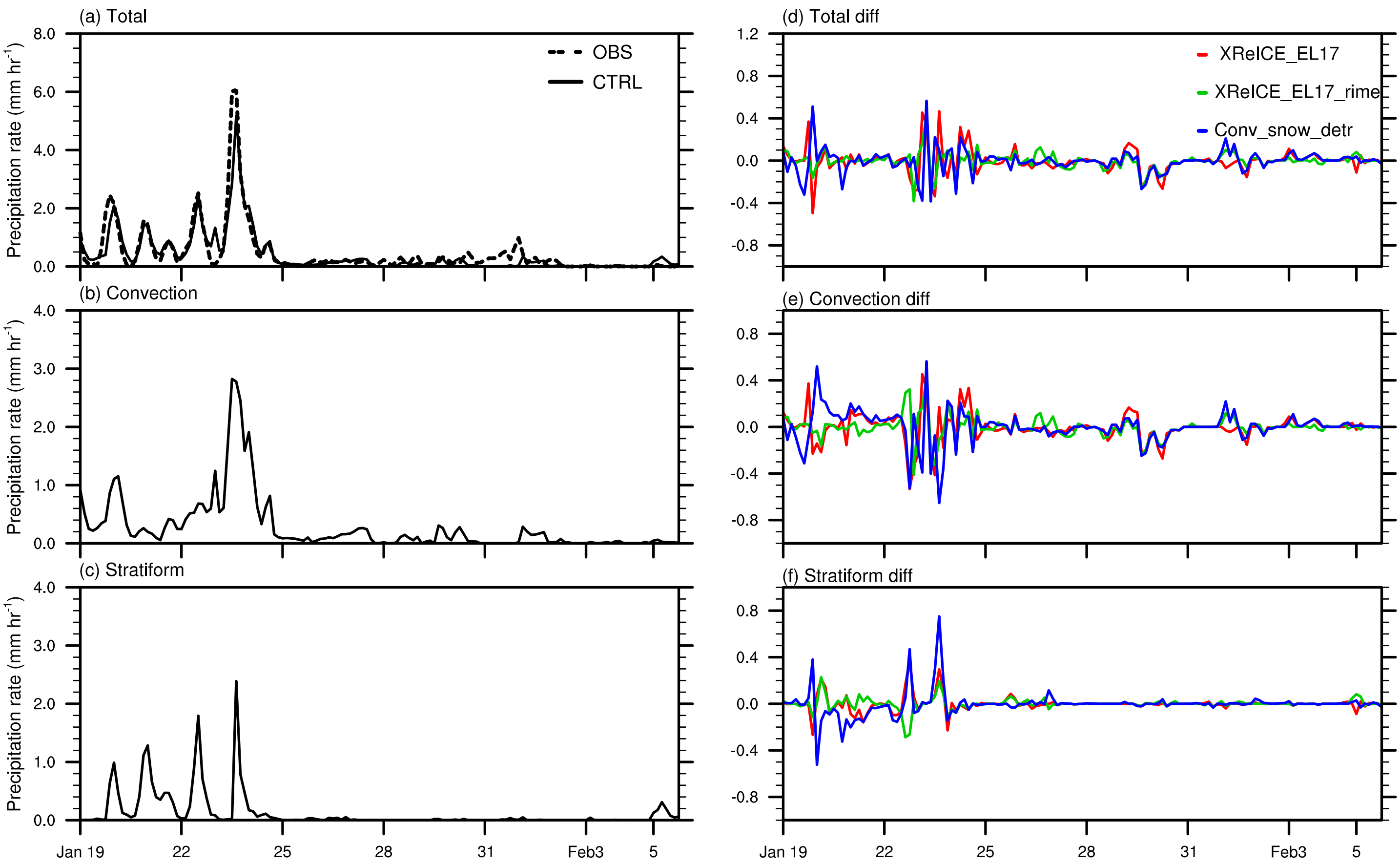
(a) Total
OBS
CTRL
(b) Convection
(c) Stratiform
(d) Total diff
XReICE_EL17
XReICE_EL17_rime
Conv_snow_detr
(e) Convection diff
(f) Stratiform diff
Precipitation rate (mm hr-1)
Jan 19
22
25
28
31
Feb3
5

Figure5.

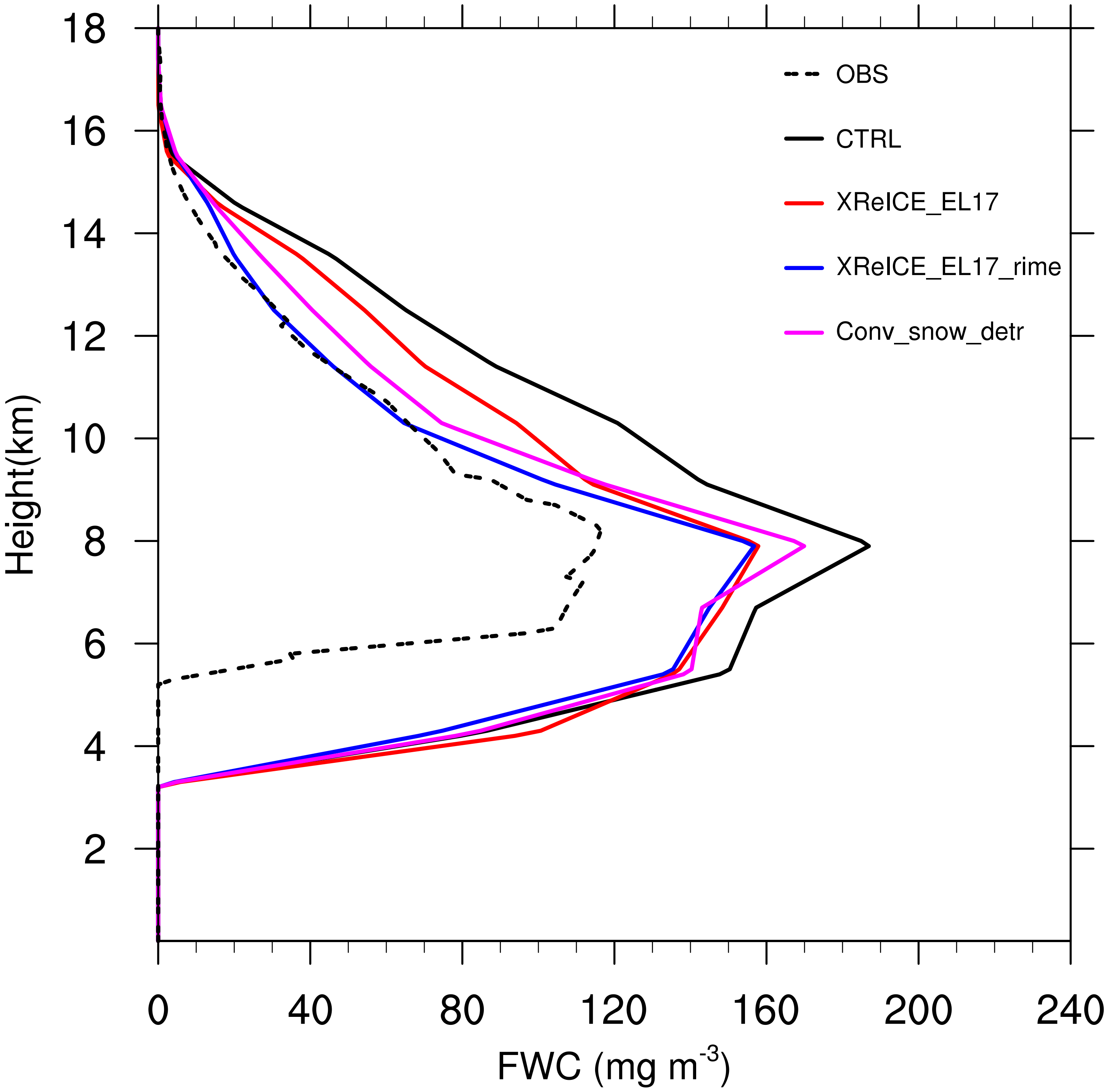
OBS
CTRL
XReICE_EL17
XReICE_EL17_rime
Conv_snow_detr
Height(km)
FWC (mg m^{-3})
0
40
80
120
160
200
240
2
4
6
8
10
12
14
16
18

Figure6.

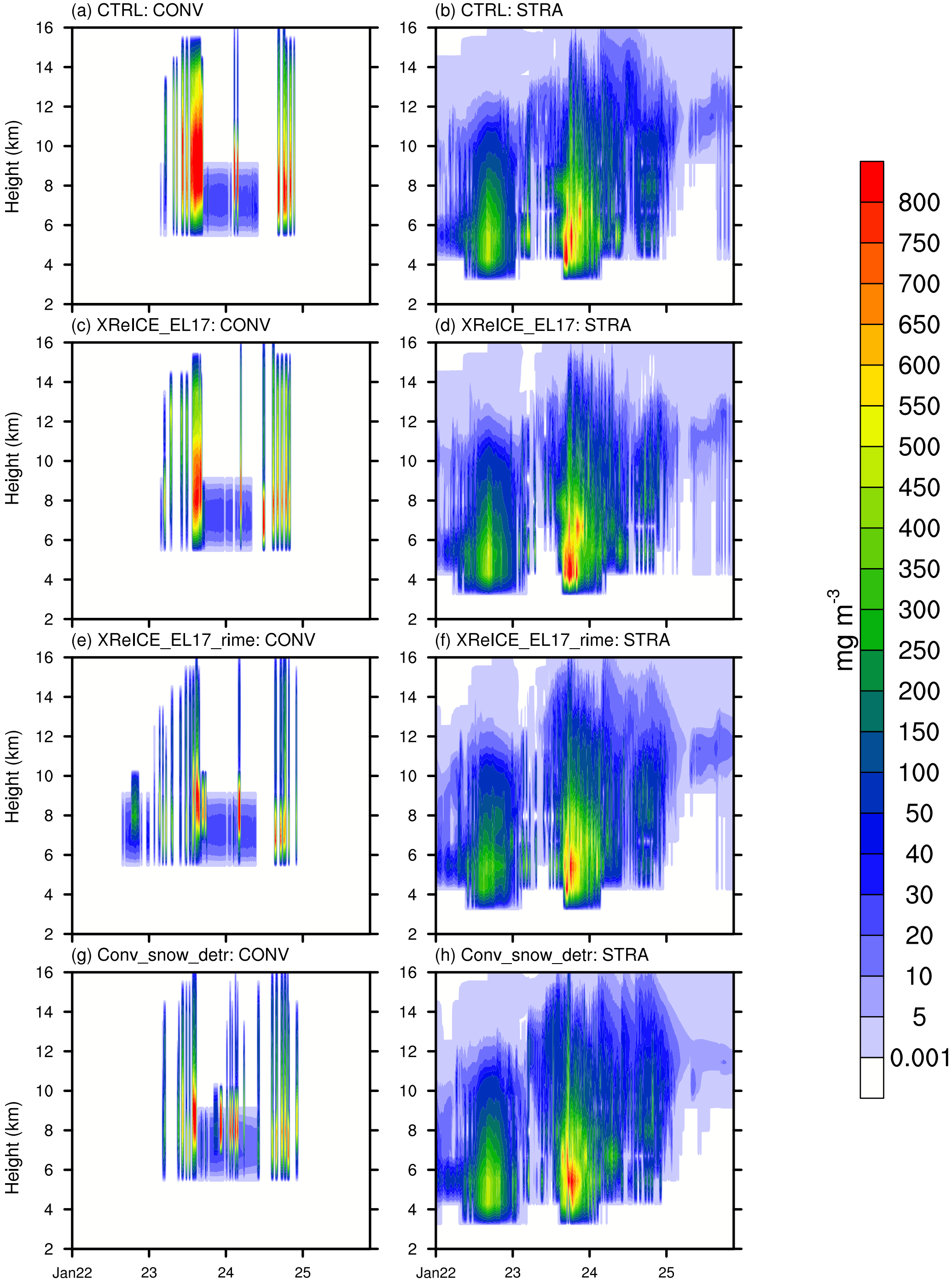
(a) CTRL: CONV
(b) CTRL: STRA
(c) XReICE_EL17: CONV
(d) XReICE_EL17: STRA
(e) XReICE_EL17_rime: CONV
(f) XReICE_EL17_rime: STRA
(g) Conv_snow_detr: CONV
(h) Conv_snow_detr: STRA
Height (km)
2
4
6
8
10
12
14
16
Jan22
23
24
25
mg m-3
0.001
5
10
20
30
40
50
100
150
200
250
300
350
400
450
500
550
600
650
700
750
800

Figure7.

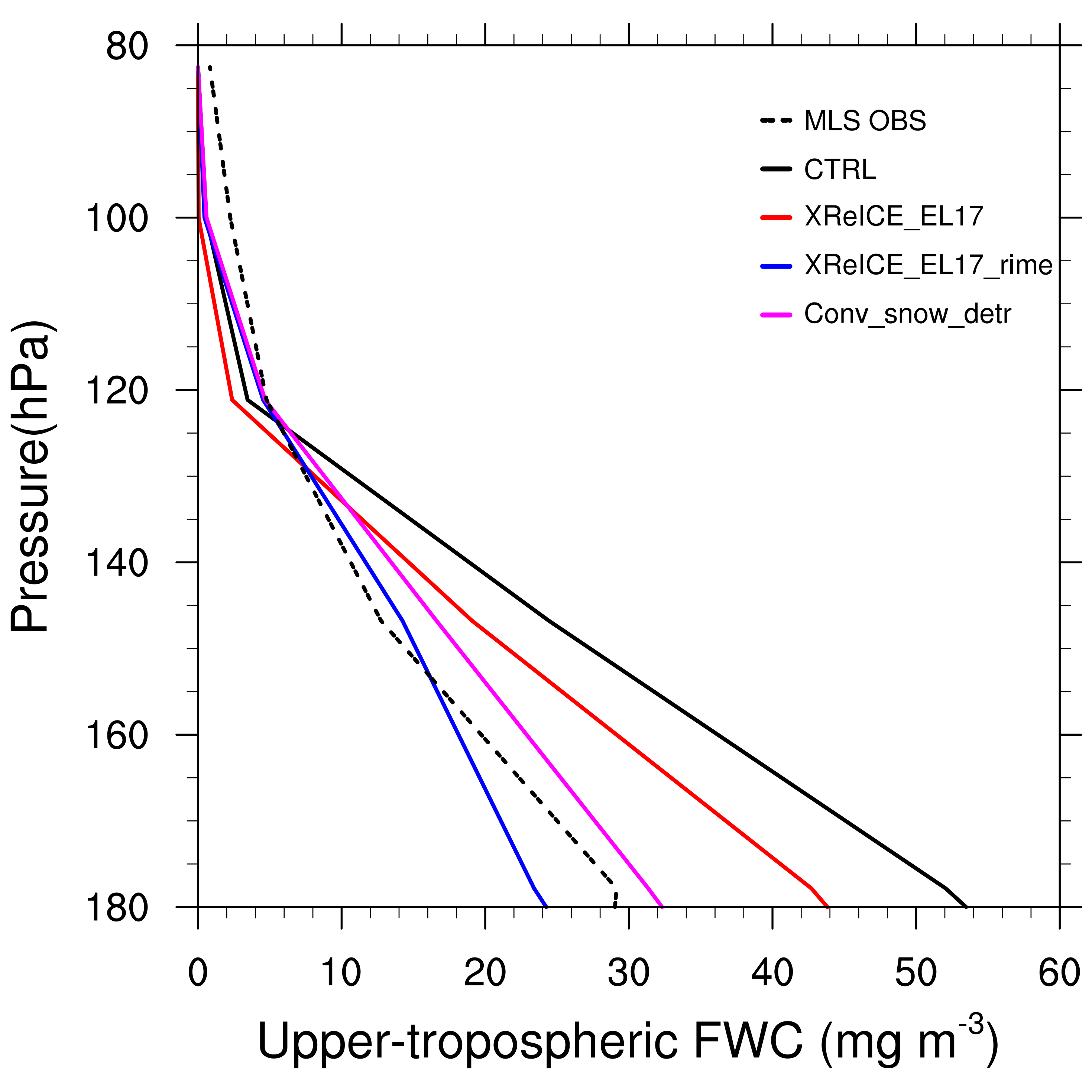

MLS OBS
CTRL
XReICE_EL17
XReICE_EL17_rime
Conv_snow_detr
Pressure(hPa)
80
100
120
140
160
180
0
10
20
30
40
50
60
Upper-tropospheric FWC (mg m-3)

Figure8.

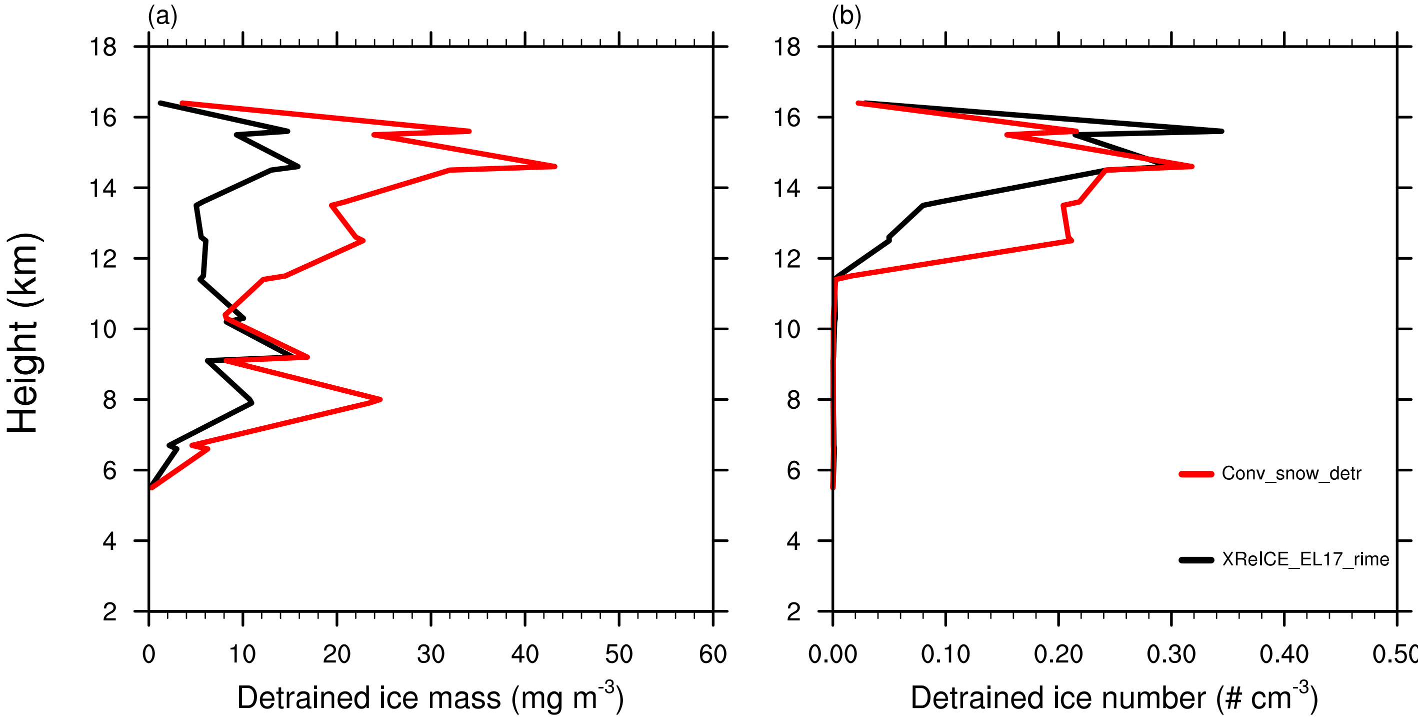

(a)
(b)
Height (km)
18
16
14
12
10
8
6
4
2
0
10
20
30
40
50
60
Detrained ice mass (mg m-3)
0.00
0.10
0.20
0.30
0.40
0.50
Detrained ice number (# cm-3)
Conv_snow_detr
XReICE_EL17_rime

Figure9.

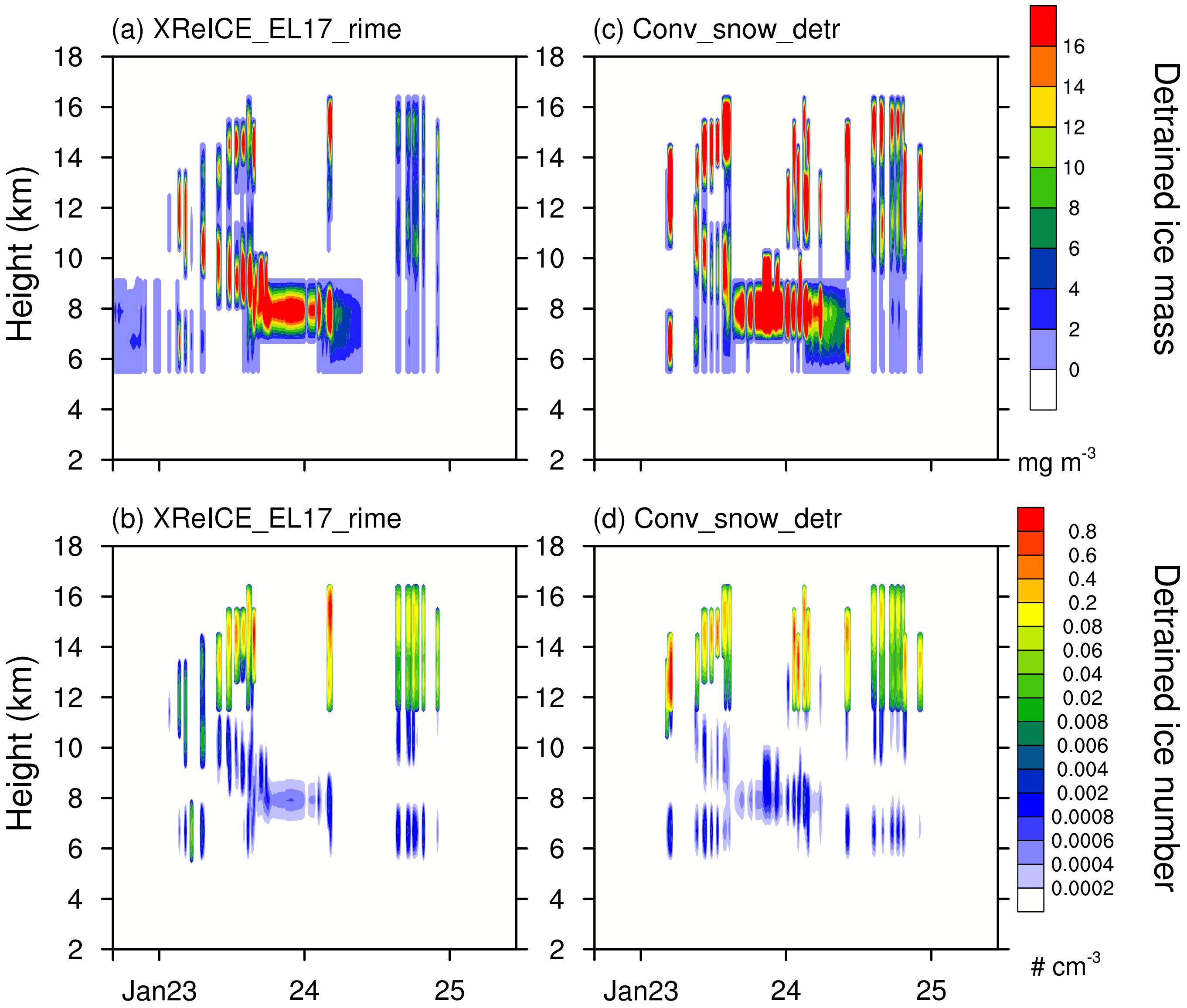
(a) XReICE_EL17_rime
(c) Conv_snow_detr
(b) XReICE_EL17_rime
(d) Conv_snow_detr
Height (km)
18
16
14
12
10
8
6
4
2
Jan23
24
25
Detrained ice mass
mg m^{-3}
16
14
12
10
8
6
4
2
0
Detrained ice number
cm^{-3}
0.8
0.6
0.4
0.2
0.08
0.06
0.04
0.02
0.008
0.006
0.004
0.002
0.0008
0.0006
0.0004
0.0002

Figure10.

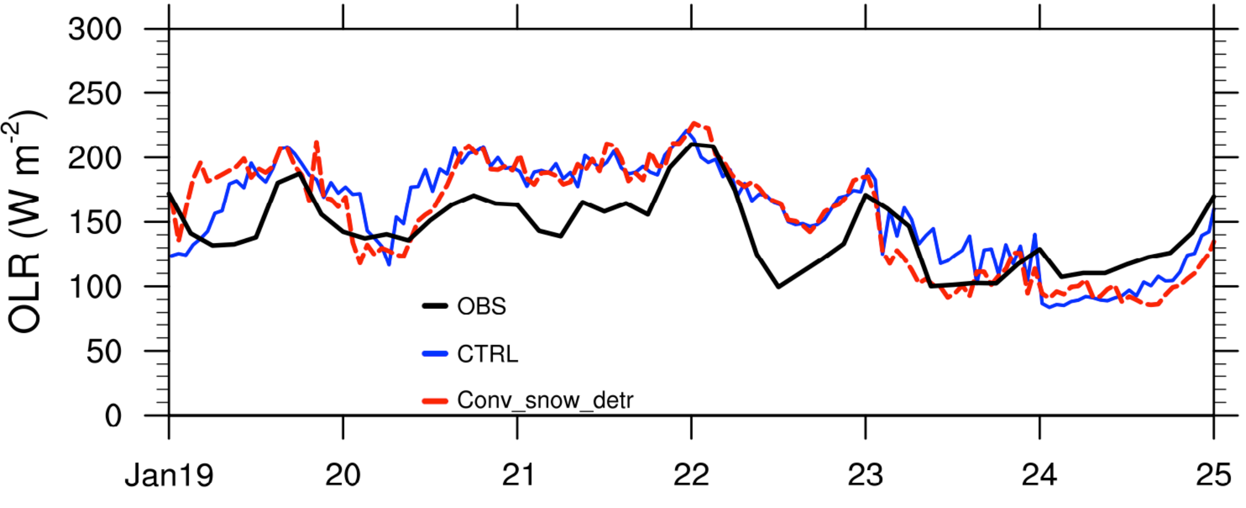
OLR (W m-2)
300
250
200
150
100
50
0
OBS
CTRL
Conv_snow_detr
Jan19
20
21
22
23
24
25

Figure11.

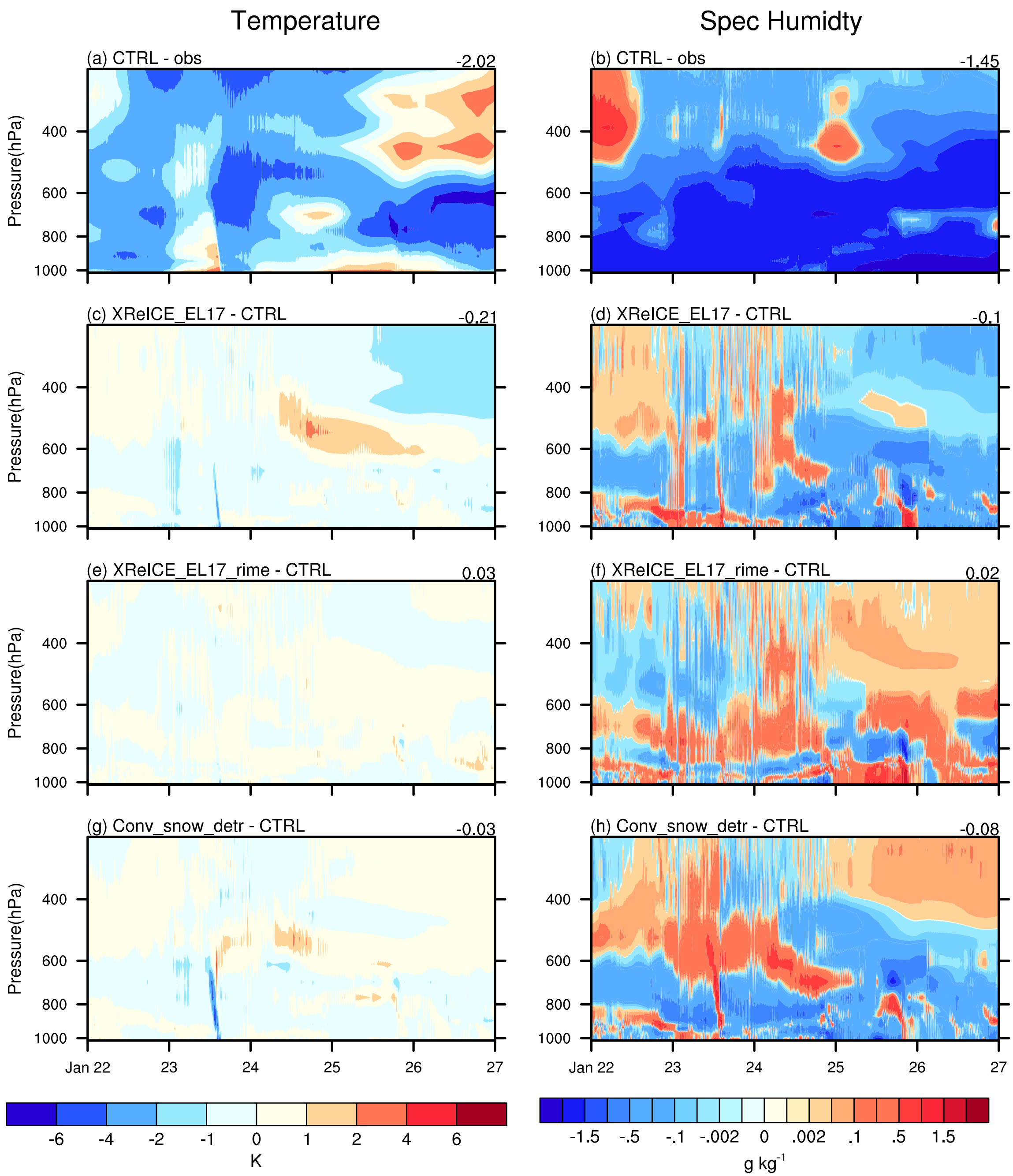

Temperature
Spec Humidty
(a) CTRL - obs
-2.02
(b) CTRL - obs
-1.45
(c) XReICE_EL17 - CTRL
-0.21
(d) XReICE_EL17 - CTRL
-0.1
(e) XReICE_EL17_rime - CTRL
0.03
(f) XReICE_EL17_rime - CTRL
0.02
(g) Conv_snow_detr - CTRL
-0.03
(h) Conv_snow_detr - CTRL
-0.08
Pressure(hPa)
400
600
800
1000
Jan 22
23
24
25
26
27
-6 -4 -2 -1 0 1 2 4 6
K
-1.5 -.5 -.1 -.002 0 .002 .1 .5 1.5
g kg-1

Figure12.

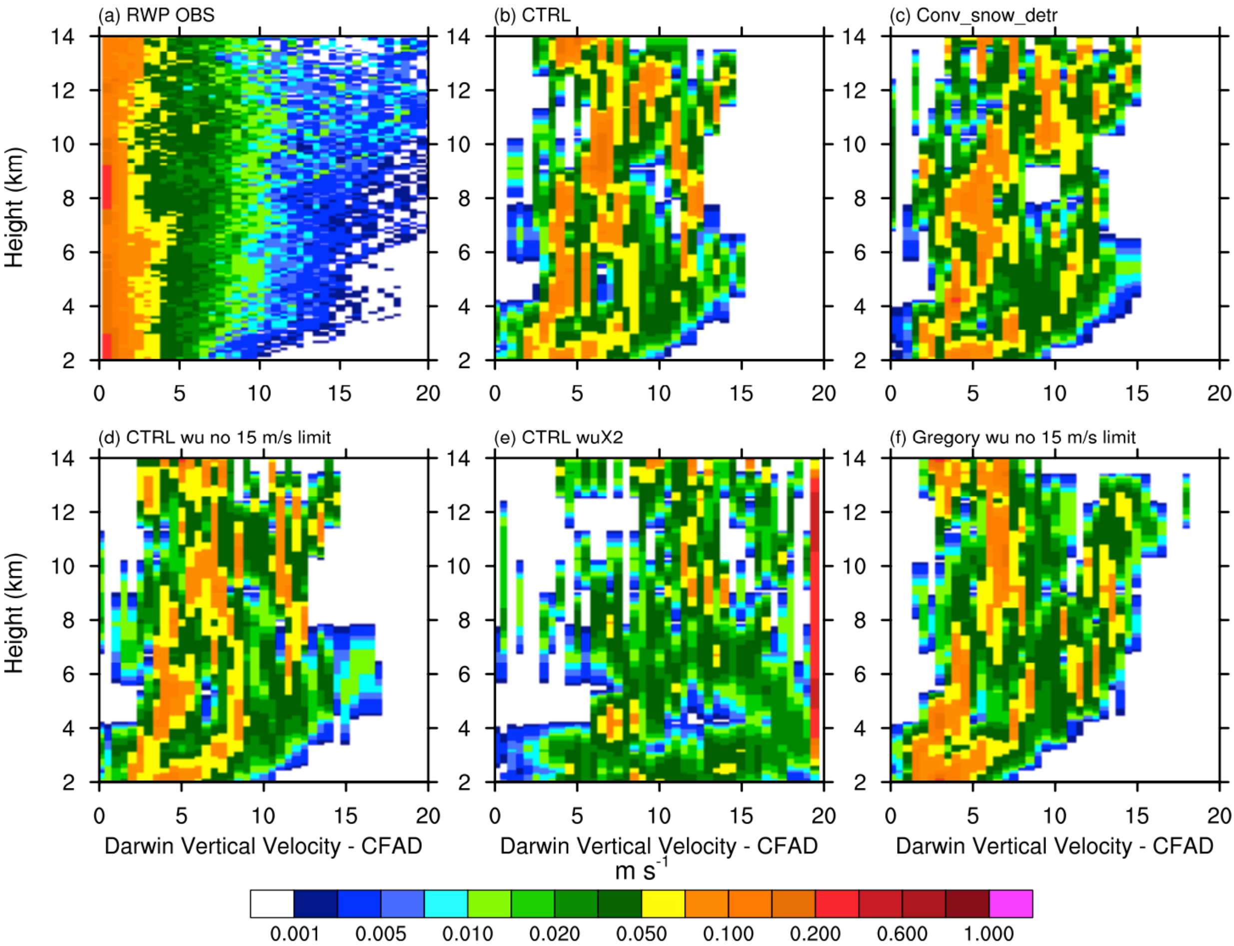
(a) RWP OBS
(b) CTRL
(c) Conv_snow_detr
(d) CTRL wu no 15 m/s limit
(e) CTRL wuX2
(f) Gregory wu no 15 m/s limit
Height (km)
Darwin Vertical Velocity - CFAD
m s-1
0.001
0.005
0.010
0.020
0.050
0.100
0.200
0.600
1.000

FigureA1.

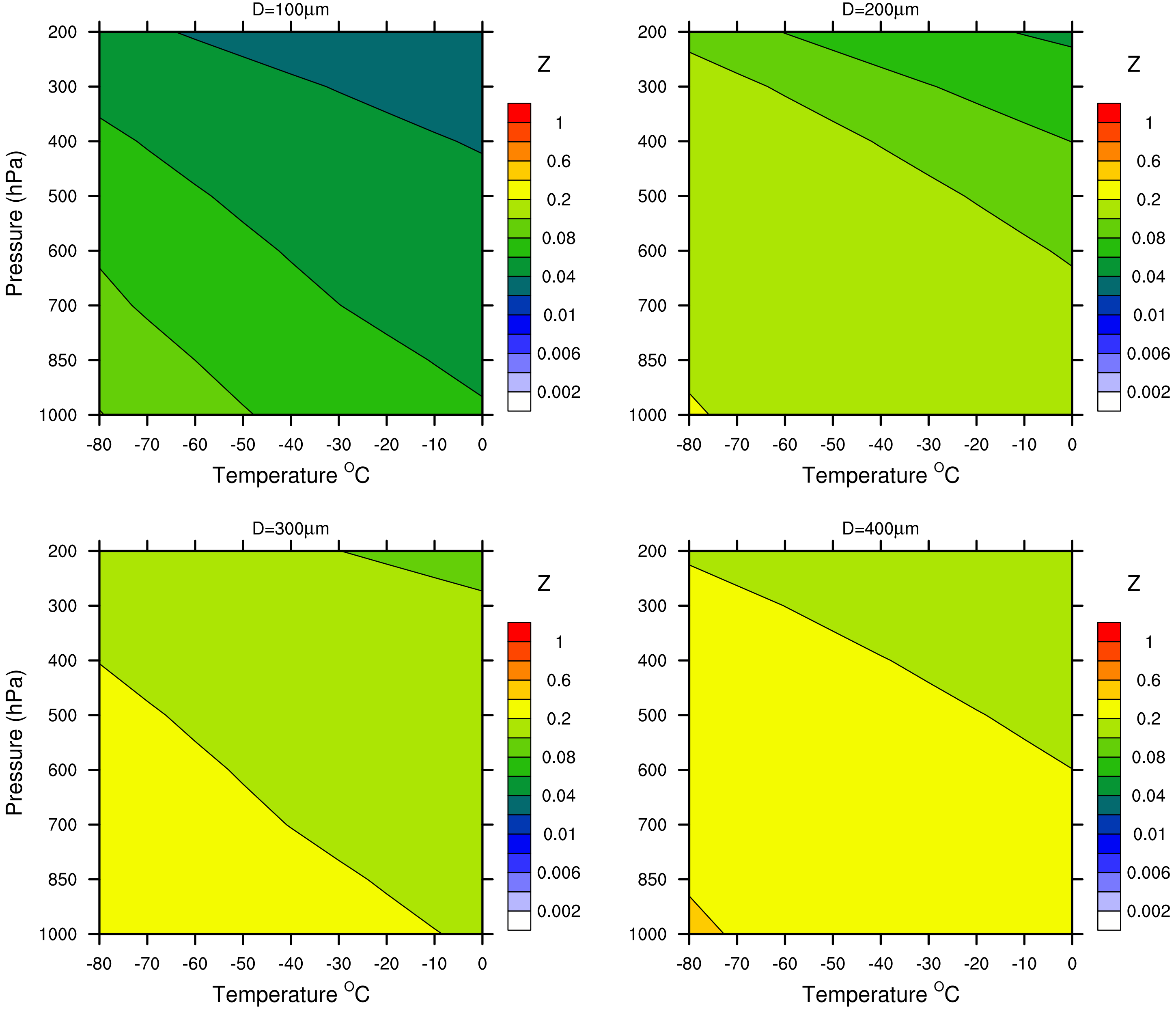

D=100µm
D=200µm
D=300µm
D=400µm
Z
1
0.6
0.2
0.08
0.04
0.01
0.006
0.002
Pressure (hPa)
200
300
400
500
600
700
850
1000
-80
-70
-60
-50
-40
-30
-20
-10
0
Temperature °C